OPTICAL CHARACTERIZATION OF THIN SCATTERING SAMPLES: APPLICATION TO BREAST CANCER RESEARCH

Garofalakis Anikitos

November 2, 2003

Contents

Chapter 1

Introduction

Biological tissue is visually opaque due to the fact that, besides from absorption there is high scattering of light. White paint, foam and milk, with their characteristic white color (due to multiple scattering), have similar behavior. As photons enter inside a scattering medium they suffer many scattering events and follow random trajectories. Light is transported in a process similar to electrons in heat diffusion. Light scattering in tissues is signifficantly dominant over absorption in the wavelengths between 600 and 1100 nm as it can be seen at Fig. 1.0.1 where the absorption spectrum of the various components of tissue is presented.

It is useful to examine what happens when a near infrared laser pulse enters inside a slab of tissue (Fig. 1.0.2). An extremely small portion of the incident light will travel in a straight line and will not experience any scattering. These photons are called ballistic. Snake photons are those that will scatter few times before they exit the slab and they follow zig-zag trajectories along the direction of propagation. Snake photons arrive later than the ballistic ones. The greatest portion of the incident photons will experience many scattering events and will appear later. These photons that are called diffusive, can give a lot of information of the medium that they travel. Diffuse photons have given rise to a new field inside the biomedical community due to their potential to probe body function and structure non-invasively.

A laser pulse is only one of the methods of illuminating the human body. In fact the use of light for medical purposes exists before the development of lasers. The use of light for body monitoring goes back to the Victorian doctors who were trying to view inside the human body by using a candlelight. Their attempts were unsuccessful since scattering was so strong that it blurred the image. The above method is known as diaphanography and has developed through the years as the light sources became more intense and the detectors became more sensitive. With the discovering of lasers, investigators used them as light sources and tried to benefit from their special characteristics i.e. spectral brightness, directionality, coherence, monochromaticity and optional short time duration.

One of the most targeted body organs in the biomedical community has been the female

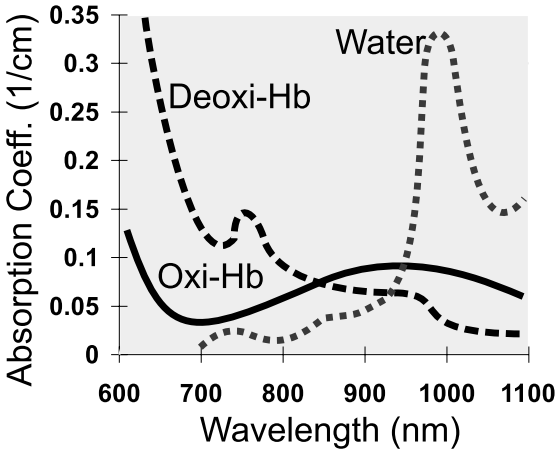

Figure 1.0.1: Absorption Spectrum

breast. Breast cancer is the second leading cause of cancer deaths in women today (after lung cancer) and is the most common cancer among women exluding nonmelanoma skin cancers. According to the World Health Organization more thatn 1.2 million people will diagnosed with breast cancer this year worldwide. There is a number f imaging techniques of thebreast (mammography) with each one having its own limitations. The best by far is the X-ray mammography which is currently used as the screening examination of choice. The test however although it has high sensitivity has a rather low specificity leading to an increased number of unnecessary biopsies. Ultrasound examination of the breast has been tested as apossible screening tool but it failed and now it is considered a complimentary to the X-ray mammography examination. Magnetic Resonance Imaging (MRI) is a quite powerful technique with submillimeter resolution but its hogh specificity is accompanied by low sensitivity. Magnetic resonance imaging cannot detect some important elements like oxygen. Other techniques using radiolabeled substances have been used to produce scinimammographies but they are still under evaluation.

Light can detect the chemistry of tissue and has been proposed as an alternative imaging technique. The main drawback of the optical method is that light scattering limits our ability to form a clear image inside the breast. Great efforts have been made so far to alleviate the above problem. The main approach is based on studying the light propagation inside a highly scattering substance like tissue.

During recent years great efforts have been made to study light scattering in turbid media mainly due to the extensive use of lasers in medicine as a therapeutic and diagnostic tool[1, 2, 3, 4, 5].Light propagation depends on the optical properties of the medium, and mainly from the scattering and the absorption coefficients. These two properties will play an important role in this work, since their value is used for the characterization of tissue. Light propagation is usually modeled by using two theories: the wave theory (Maxwell's equations) and the transport

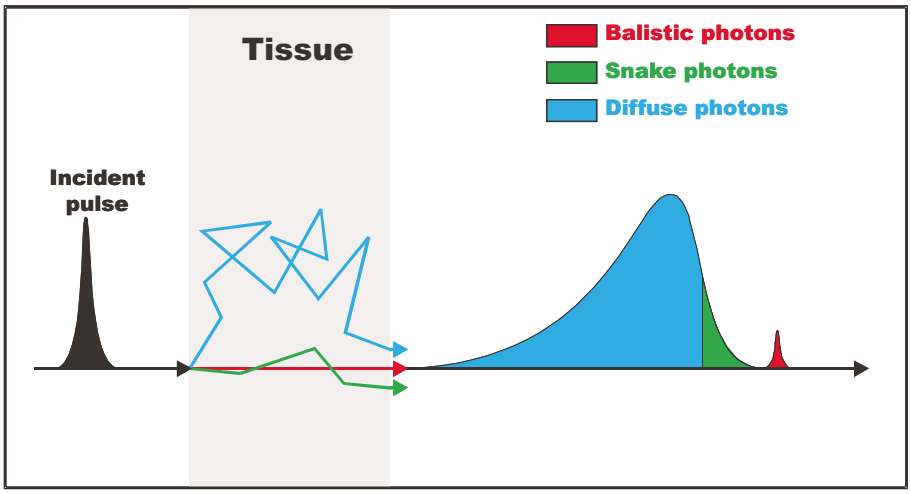

Figure 1.0.2: Transmitted pulse pulse from a high scattering medium

theory. On wave theory, the Maxwell equations need to be solved for the substance of interest and the optical properties are defined via the dielectric constant $\varepsilon(\mathbf{r})$. The real part of $\varepsilon(\mathbf{r})$ is related with scattering, while the imaginary part represents the absorption. In most practical systems, solving the Maxwell equations is extremely complicated. On the other hand, theoretical research in tissue optics has been based on the Radiative Transfer Equation (RTE) [6, 7]or approximations to it where analytical solutions are easily extracted[1]. In transport theory, light is treated as energy propagating according to the rules defined by the Radiative Transfer Equation.

The most common approach is based on the diffusion approximation [7] in which the light inside a scattering medium is assumed to be diffusive [8]. The diffusion approximation provides simple analytical expressions for light transport and can be applied to a great variety of scattering systems permitting their optical characterization. Optical characterization of a medium is the extraction of its optical properties such as scattering, absorption and the anisotropy factor [9].

By analyzing these optical properties, important information of the material may be obtained. One of the main purposes of tissue optics is to correlate the optical properties with the physiology of tissue providing a way to discriminate normal from abnormal tissue. Photon-migration techniques based on diffusion theory have been used to monitor optical properties that reflect the physiological state of tissue [10, 11, 12].

Optical characterization is a procedure that has to be divided into two parts. These are known as the forward and the inverse problem. In order to explain the two problems it is useful to examine the example of a scattering medium that is illuminated by a light source of known spatial and time distribution of Intensity. The forward problem is, given the optical properties of the medium to predict the Intensity at any place and any time inside the medium. The inverse problem is to deduce the optical properties of the medium given the measurements

of Intensity and with the aid of the incident source distribution. For the characterization of a medium both the forward and the inverse problem are necessary. In the forward problem assumptions are made that have to do with the propagation of light inside a scattering medium. Several models are developed and are experimentally tested. After the validation of a theory, the inverse problem uses the expressions of the forward problem in order to extract the optical properties through fitting procedures.

Optical characterization is also an important process when we perform optical imaging. Generally, the detection of cancer can be viewed as a three-step procedure: detection, localization and characterization of the tumor. In order to pin-point tumor tissue by means of an in-vivo optical measurement, its properties must firstly characterized ex-vivo. This is the first objective of this work i.e. to characterize a large number of breast tumor biopsies.

Moreover, the medical utility of optical imaging depends on whether the measured optical contrast provides enough information to differentiate normal from abnormal tissue. In optical imaging the detection of an inhomogeneity inside the breast is performed due to its different optical properties from the normal background. Up to now, in-vivo images of tumors are based on contrast provided by the absorption coefficient [4, 5]. This work tries to examine the potential of imaging due to changes of the scattering coefficient and thus both cancerous and normal tissue samples were characterized according to their scattering coefficient. This will be the second objective of this work: relating the scattering coefficient of tissue with its physiological state.

Biopsies are small in size ($< 5\,mm$) and the difusion equation that is commonly used cannot be applied on such systems of small thickness. The characterization of optically thin scattering samples, i.e. scattering samples with sizes comparable to the transport mean free path (l_{tr}) has not received much attention. When dealing with small system sizes the common approach is to employ Monte Carlo simulations [13, 14, 15, 16] or solutions to the RTE [17, 18, 19, 20, 21]. However, when a large number of different samples need to be characterized the use of computationally expensive methods such as Monte Carlo or RTE solvers is, at the present moment, impractical. In these cases a simple analytical expression valid for a large range of sizes would be preferable [22].

Furthermore, an important issue for imaging is the spatial resolution that each technique can provide. Diffuse Optical tomography is based on the difusion approximation. Thus, the spatial resolution of images resulting from diffusion equation analysis is anavoidably limited to several transport mean free paths. Expanding the range of validity of the diffusion approximation to limiting cases such as small samples, short times, or in the presence of high absorption [23, 24, 25] will increase our ability to characterize scattering media. In particular, simple analytical solutions to the diffusion equation that deliver accurate results in limiting cases [26]will provide a means to image in scattering media with sizes comparable to l_{tr}, increasing

the range of application of diffuse optical tomography [2, 3, 4, 5] , optical mammography [27, 28]and fluorescence- mediated molecular tomography [29, 30, 31, 32].A new theory needs to be developed that can treat systems of small thickness in a fast way, this is the third and final aim of this work.

Chapter 2 presents the fundamentals of the widely accepted diffusion theory. Solutions to simple geometries are also presented and the limitations of the existing theories are discussed. In Chapter 3 modifications to the standard diffusion equation in order to hold for small geometries, are presented together with an analytical expression for the case of a diffusive slab. In Chapter 4, the experimental configuration and the subjects of the present study are presented. Chapter 5 describes the approach being used for solving the inverse problem. Moreover the limits of the modified theory are explored together with a comparison of the existing theories. In Chapter 6, characterization of a large number of tissues is performed according to their reduced scattering coefficient. Finally Chapter 7 concludes the findings of this work.

Chapter 2

The Diffusion Equation

In this chapter the principles that govern the light transport within the diffusion equation are presented. The basic steps folowed in order to reach the diffusion equation from the Radiative Transfer Equation are presented. To do so, the Diffusion Approximation and its limitations are also introduced.

2.1 Radiative Transfer Equation

The photon propagation in highly scattering media is modeled with the use of the Boltzman transport equation for the light which is also known as Radiative Transfer Equation (RTE)[7, 6, 33]

$$\frac{n}{c}\frac{\partial I\left(\mathbf{r},\hat{\mathbf{s}}\right)}{\partial t}=-\hat{\mathbf{s}}\cdot\nabla I\left(\mathbf{r},\hat{\mathbf{s}}\right)-\mu_{t}I\left(\mathbf{r},\hat{\mathbf{s}}\right)+\frac{\mu_{t}}{4\pi}\int_{4\pi}p\left(\hat{\mathbf{s}},\hat{\mathbf{s}}'\right)d\Omega'+\epsilon\left(\mathbf{r},\hat{\mathbf{s}}\right) \tag{2.1.1}$$

where $I\left(\mathbf{r},t\right)$ is the specific intensity that represents the average power flux at position $\mathbf{r}$, propagating along the unit vector $\hat{\mathbf{s}}$ with units $Wcm^{-2}sr^{-1}$(sr = steradian = unit solid angle)and μ_t is the total macroscopic cross section with units of cm^{-1}. The phase function $p(\hat{\mathbf{s}},\hat{\mathbf{s}}')$ represents the probability of scattering into a direction $\hat{\mathbf{s}}'$ from a direction $\hat{\mathbf{s}}$. Finally $\epsilon\left(\mathbf{r},s\right)$ is the spatial and angular distribution of the source.

The RTE is conservation equation for the specific Intensity inside a small volume element and in the direction $\hat{s}$. The first term on the right hand side describes the loss over the boundary of dV, the second term the losses due to absorption and scattering , the third term any gain due to scattering from other directions into $\hat{s}$ and the last term the gains due to any source inside dV.

If we now integrate over all 4π of solid angle in the RTE we will obtain:

$$\frac{1}{c}\frac{\partial}{\partial t}\int_{4\pi}I\left(\mathbf{r},\hat{\mathbf{s}}\right)d\Omega=-\nabla\cdot\int_{4\pi}I\left(\mathbf{r},\hat{\mathbf{s}}\right)\hat{\mathbf{s}}d\Omega-\mu_{a}\int_{4\pi}I\left(\mathbf{r},\hat{\mathbf{s}}\right)d\Omega+\int_{4\pi}\epsilon\left(\mathbf{r},\hat{\mathbf{s}}\right)d\Omega, \tag{2.1.2}$$

In equation (2.1.2) we can recognise some interesting radiometric quantities. The $averageintensityU$ and *total flux density* $\mathbf{J}$ are defined in terms of the specific Intensity as:

$$U(\mathbf{r}) = \int_{4\pi} I(\mathbf{r}, \hat{\mathbf{s}})\, d\Omega \tag{2.1.3}$$

$$\mathbf{J}(\mathbf{r}) = \int_{4\pi} I(\mathbf{r}, \hat{\mathbf{s}})\, \hat{\mathbf{s}} d\Omega. \tag{2.1.4}$$

Both the *average intensity* U and *total flux density* $\mathbf{J}$ have units $[W/cm^2]$.

Inserting the quantities $U(\mathbf{r})$ and $\mathbf{J}(\mathbf{r})$ into eq. (2.1.2), we obtain the equation of flux conservation:

$$\frac{1}{c}\frac{\partial U(\mathbf{r})}{\partial t} + \nabla \cdot \mathbf{J}(\mathbf{r}) + \mu_a U(r) = E(\mathbf{r}) \tag{2.1.5}$$

In eq. (2.1.5) we define:

$$E(\mathbf{r}) = \int_{4\pi} \epsilon(\mathbf{r}, \hat{\mathbf{s}})\, d\Omega \tag{2.1.6}$$

measured in $[Wcm^{-3}]$, as the power generated per unit volume.

2.1.1 Transport Properties

In this subsection the quantities presented in the RTE are discussed furthermore. We will start with the macroscopic cross-section μ_t which is also called transport coefficient or total attenuation coefficient. The macroscopic cross-section has units of $[cm^{-1}]$ and is defined as:

$$\mu_t = \rho(\sigma_a + \sigma_s) \tag{2.1.7}$$

In the above equation ρ is the density of scatterers while $\sigma_a$and σ_s are the absorption and scattering cross-section respectively, measured in $[cm^2]$.The transport coefficient can be also be written as:

$$\mu_t = \mu_s + \mu_a\ . \tag{2.1.8}$$

In the above equation μ_s is the scattering coefficient. The scattering coefficient is the multiplicative inverse of the random-walk step length (which is also known as the scattering mean free path or just mean free path):

$$\mu_s = \frac{1}{l_{tr}} \tag{2.1.9}$$

where l_{sc} is equal to the characteristic distance between two scattering events.

Analogue to the scattering mean free path, the absorption length is defined in terms of the absorption coefficient $\mu_a$as:

$$l_a = \frac{1}{\mu_a} \,. \tag{2.1.10}$$

The absorption length is the average distance that a photon undergoes before it is absorbed.

In the eq. (2.1.1) the phase function $p\left(\hat{\mathbf{s}}, \hat{\mathbf{s}}'\right)$was also presented. The phase function (also known as probability density function) represents the probability that a photon will scatter into a direction $\hat{\mathbf{s}}'$ from a direction $\hat{\mathbf{s}}$. The phase function holds the following relationship:

$$\frac{1}{4\pi} \int_{4\pi} p\left(\hat{\mathbf{s}}, \hat{\mathbf{s}}\right) d\Omega = \frac{\mu_s}{\mu_t} = W_0 \,, \tag{2.1.11}$$

where W_0 is called albedo. In biological tissues it is a common approach to assume that the phase function depends only on the angle between $\hat{\mathbf{s}}$ and $\hat{\mathbf{s}}'$, i. e. $p\left(\hat{\mathbf{s}}, \hat{\mathbf{s}}'\right) = p\left(\hat{\mathbf{s}} \cdot \hat{\mathbf{s}}'\right) = p\left(\cos\theta\right)$, and is often approximated in the following form:

$$p\left(\cos\theta\right) = \frac{W_0\left(1 - g^2\right)}{\left(1 + g^2 - 2g\cos\theta\right)^{3/2}} \tag{2.1.12}$$

The above equation is the well-known Henyey-Greenstein formula, and constitutes the most commonly used approximation for the phase function in biological media. In the eq. (2.1.12), g is the average cosine of the scattering angle and it is defined in terms of the phase function as:

$$g = <\cos\theta> = \frac{\int_{4\pi} p\left(\hat{\mathbf{s}} \cdot \hat{\mathbf{s}}'\right) \hat{\mathbf{s}} \cdot \hat{\mathbf{s}}' d\Omega'}{\int_{4\pi} p\left(\hat{\mathbf{s}} \cdot \hat{\mathbf{s}}'\right) d\Omega'} \,. \tag{2.1.13}$$

According to its definition, g is a quantity which express the anisotropy of the scattered light on interaction with the particle, and as such, is called the anisotropy factor. Typical values in tissue range from 0.8 to 0.9.

2.2 Diffusion Approximation

Mathematically, the use of the RTE for tissue measurements imposes several practical limitations due to its integro-differential nature. Analytic solutions of the transport equation are difficult to obtain and numerical calculations require large amounts of computational power. Solutions typically exist only for simple geometries like spheres, cubes, planes and cylinders.

Therefore approximations have been developed to convert the transport equation to more manageble but functional forms. A standard approximation method expands the specific intensity I at point $\mathbf{r}$ flowing in direction $\hat{\mathbf{s}}$, in a series of spherical harmonics. If this expansion is limited to the first two terms, this consists the P1 approximation.

$$I\left(\mathbf{r},\hat{\mathbf{s}},t\right)\simeq\frac{1}{4\pi}U_t\left(\mathbf{r},t\right)+\frac{3}{4\pi}\mathbf{J}_t\left(\mathbf{r},t\right)\cdot\hat{\mathbf{s}} \tag{2.2.1}$$

where U_t is the time dependent average intensity, and $\mathbf{J}_t$ represents the flux.

This approximation reduces the eq. (2.1.1) into more simple equations where analytical expressions can be derived.The diffusion approximation assumes that the average intensity inside the scattering medium can be considered diffusive. This is actually the case in a medium, when the phase function is not too anisotropic and we are away from sources and boundaries.

If we substitute eq. (2.2.1) into eq. (2.1.1), multiply by $\hat{\mathbf{s}}$ and integrate over 4π we obtain:

$$\nabla U\left(\mathbf{r}\right)=-3\left(\mu_s'+\mu_a\right)\mathbf{J}\left(\mathbf{r}\right)-3\frac{n}{c}\frac{\partial\mathbf{J}\left(\mathbf{r}\right)}{\partial t}+\int\epsilon\left(\mathbf{r},\hat{\mathbf{s}}\right)\hat{\mathbf{s}}d\Omega \tag{2.2.2}$$

We will assume that source is isotropic, i.e. the intensity generated does not depend on $\hat{\mathbf{s}}$. Then the last term in eq. (2.2.2) can be neglected:

$$\nabla U_t\left(\mathbf{r},t\right)=-3\mu_s'\left[\frac{n_0}{c\mu_s'}\left(\frac{\partial}{\partial t}+\frac{c\mu_a}{n_0}\right)+1\right]\mathbf{J}_t\left(\mathbf{r},t\right) \tag{2.2.3}$$

In eqs. (2.2.2),(2.2.3), μ_s' is the reduced scattering coefficient, defined as:

$$\mu_s'=\mu_s\cdot\left(1-g\right)\ . \tag{2.2.4}$$

In terms of μ_s', we shall define the transport mean free path l_{tr}:

$$l_{tr}=\frac{1}{\mu_s'}=\frac{l_{sc}}{1-g}\ . \tag{2.2.5}$$

which includes the anisotropy factor g .

The reduced scattering coefficient takes into account the anisotropy of the scattering. This can be understood if we consider that the transport mean free path $(1/\mu_s')$ is the average distance that a photon travels before its propagation direction is completely randomized by a series of scattering events. In other words, $1/\mu_s'$ defines a distance where the scattering can be regarded as isotropic.

The reduced scattering coefficient and the absorption coefficient are the optical parameters that are primarily used for tissue characterization. The magnitude of μ_s' in a tissue is determined in part by the concentration of micron-sized optical heterogeneities, such as the cell organelles while the absorption coefficient μ_a depends on the concentration and absorption cross-section of various chromophores, such as the hemoglobin that resides in blood vessels.

2.2.1 Fick's Law

As presented in the previous section, if Eq. 2.2.1 is introduced in the time-dependent expression for the Radiative Transfer Equation, one finally reaches the expression for an isotropic source in a medium with absorption coefficient μ_a, reduced scattering coefficient μ_s' and index of refraction n_0 (Eq. (2.2.3)). In Eq. (2.2.3) we find two characteristic times:

$$t_{tr} = \frac{n_0}{\mu_s'} = \frac{n_0}{c} l_{tr} \tag{2.2.6}$$

being t_{tr} the average time required to travel the transport mean free path distance, and

$$t_a = \frac{n_0}{c\mu_a} \tag{2.2.7}$$

being t_a the characteristic time of flux $\mathbf{J}$ to change due to absorption. A common approach is to assume that variations in the diffuse total flux take place over a time scale much larger than the lapse between scattering events on particles on the medium, and also that the time of change of the total flux due to absorption is much larger than the time between scattering events ($t_{tr} \ll t_a$). Introducing these approximations in Eq. (2.2.3) we obtain:

$$\mathbf{J}(\mathbf{r}) = -\frac{1}{3\mu_s'} \nabla U(\mathbf{r}) \ . \tag{2.2.8}$$

which is Fick's law for diffusion of the average intensity.

Fick's law can be also seen as:

$$\mathbf{J}(\mathbf{r}) = -\frac{1}{3(\mu_s' + a\mu_a)} \nabla U(\mathbf{r}) \ , \tag{2.2.9}$$

where from this derivation a is 1 or 0 depending if we consider t_a or not (the main difference between Ishimaru's and Furutsu's theories [34]). From Eq. (2.2.9) one directly obtains a time-independent expression for the diffusion coefficient:

$$D = \frac{1}{3(\mu_s' + a\mu_a)} \tag{2.2.10}$$

The dependence of the diffusion coefficient with absorption is a controversial issue and will not be dealt with here [23, 24, 25, 35, 36, 37]. Within this work we shall use the formula presented in Ref. [23], which we have verified with Monte Carlo simulations, yielding very accurate results even in the presence of extremely high absorption. In all instances presented in this work we have found that $a \sim 0.2$, with variations smaller than 1%.

2.3 Diffusion Equation

There are several modifications of the diffusion equation depending the approximations taken through its derivation. In fact, the approximations taken on eq. (2.2.3) determine the different expressions that diffusion equation may have, and the different expressions of the diffusion coefficient D. The limits of validity of the different diffusion equations have been studied in different papers and there exist a controversy for the best expression. In this section we will start from eq. (2.2.3)and we will apply several approximations to it.

No approximation

In this case, we directly apply eq. (2.2.3) into the general expression for flux conservation , eq. (2.1.5):

$$3D_1\left(\frac{n}{c}\right)^2\frac{\partial^2 U(\mathbf{r})}{\partial t^2}+\frac{n}{c}\frac{\partial U(\mathbf{r})}{\partial t}-D_1\nabla^2 U(\mathbf{r})+3\left(\mu_s'+\mu_a\right)\mu_a D_1 U(\mathbf{r})=q(\mathbf{r})\ , \tag{2.3.1}$$

where $q(\mathbf{r})=3\left(\mu_s'+\mu_a\right)D_1E(\mathbf{r})+3D_1\left(n/c\right)\partial E/\partial t$ and the diffusion coefficient $D_1$is defined as:

$$D_1=\frac{1}{3\left(\mu_s'+2\mu_a\right)} \tag{2.3.2}$$

Eq. (2.3.1) is known as telegraph equation.

2.3.1 Slow flux variation

In this case, the time derivative $\partial/\partial t$ on eq. (2.2.3)is negleted by assuming that flux variations in the diffuse total flux take place over a large time scale. To do so, the following condition must hold:

$$\frac{n}{c\mu_s'}\frac{\partial}{\partial t}\ll 1\ \Rightarrow\ \frac{\partial}{\partial t}\ll\frac{1}{n/c\mu_s'}\,. \tag{2.3.3}$$

If we apply $U(\mathbf{r},t)=U(\mathbf{r})\exp\left[-i\omega t\right]$ in eq. (2.2.3) the time derivative $\partial/\partial t$ will give: $-i\omega$. Since the modulation frequency ω has an experimental value in the order of $\omega\sim 10^8 Hz$ and the quantity $1/\left(n/c\mu_s'\right)$has values in the order of $10^{11}Hz$,then the slow flux variation is a valid approximation. The diffusion equation derived is:

$$\frac{n}{c}\frac{\partial U(\mathbf{r})}{\partial t}+D_2\nabla^2 U(\mathbf{r})+\mu_a U(\mathbf{r})=E(\mathbf{r}) \tag{2.3.4}$$

with the following diffusion coefficient:

$$D_2 = \frac{1}{3\left(\mu_s' + \mu_a\right)} \,. \tag{2.3.5}$$

This equation was presented by Patterson in ref. [9], and is one of the most commonly used expressions

2.3.2 Slow flux variation and low absorption rate

In this case, we further assume that the variations of the total flux due to absorption occur in a time scale much larger than the time between scattering events:

$$\frac{\mu_a c/n}{\mu_s' c/n} \ll 1 \tag{2.3.6}$$

which holds for typical tissue values of $\mu_a$and μ_s' . The diffusion equation in this case is written as:

$$\frac{n}{c}\frac{\partial U\left(\mathbf{r}\right)}{\partial t} + D_3 \nabla^2 U\left(\mathbf{r}\right) + \mu_a U\left(\mathbf{r}\right) = E\left(\mathbf{r}\right) \,. \tag{2.3.7}$$

with a diffusion coefficient:

$$D_3 = \frac{1}{\mu_s'} \,, \tag{2.3.8}$$

and was presented by Furutsu [38].

2.3.3 Comparing the different expressions

Although the telegraph equation has arisen from no approximation to the eq. (2.2.3) and is expected to be applicable in a greater number of cases, deriving expressions for the boundary conditions is not straightforward, and it is not commonly used. Comparing then the remaining expressions (2.3.4),(2.3.7) their only difference is on the diffusion coefficient. The dependence of the diffusion coefficient from the absorption coefficient was discussed on section 2.2.1 when the Fick's law was presented. The main drawback of both eq.(2.3.4) and (2.3.7) is that it predicts that diffusion begins instantly and thus cannot be applied on short times and small lengths. This issue will de discussed in detail on section 3.1 where a time-dependent D will be introduced.

2.4 Solutions to the diffusion equation

The Diffusion equation that we will adopt for the rest of this work referring to the standard diffusion equation is:

$$\frac{1}{c}\frac{\partial U(\mathbf{r})}{\partial t} - D\nabla^2 U(\mathbf{r}) + \mu_a U(\mathbf{r}) = E(\mathbf{r}) \ . \tag{2.4.1}$$

In general there are three different types of methods that have been considered for imaging, depending on the type of laser used as a light source: continuous wave (CW), intensity-modulated and pulsed time. It is useful to examine the solutions of the diffusion equation in the case of an infinite medium for the different types of source terms.

2.4.1 Intensity modulated source (Diffuse Photon Density Waves)

When the source of photons in a scattering medium is intensity modulated then the photon fluence inside the medium will oscillate at the same frequency. These scalar-damped traveling disturbances of light energy propagation that are created are called Diffuse Photon Density Waves (DPDW)[39]. Microscopically, individual photons undergo a random walk within the medium, but collectively, a spherical wave of photon density is produced and propagates outward from the source. The DPDWs are characterized by a well defined wavelength, group velocity and decay length and have shown their potential in detecting hidden objects inside a turbid medium[40]. The theory of DPDW is presented below together with their special characteristics.

As it was mentioned before, DPDWs are driven by an oscillating source inside the turbid medium. Let us assume that the source term is intensity modulated at a frequency ω:

$$E(\mathbf{r},t) = S_0(\mathbf{r}) + S_0(\mathbf{r})\exp[-i\omega t] \tag{2.4.2}$$

If we use 2.4.2 as the source part in eq. (2.4.1) we shall expect the solution to be written as

$$U(\mathbf{r},t) = U_{DC}(\mathbf{r}) + U_{AC}(\mathbf{r})\exp[-i\omega t] \tag{2.4.3}$$

We will solve the problem by concerning only the time dependent part. Disturbances from continuous-wave sources can be derived from the time dependent solutions by setting ω equal to zero. The diffusion equation of the frequency dependent component obeys the well known Helmholtz equation:

$$\nabla^2 U_{AC}(\mathbf{r}) + \kappa_0^2(\mathbf{r})\, U_{AC}(\mathbf{r}) = -\frac{S_0(\mathbf{r})}{D(\mathbf{r})} \tag{2.4.4}$$

where $\kappa_o$is a complex wavenumber:

$$\kappa_0(\mathbf{r}) = \sqrt{-\frac{\mu_a(\mathbf{r})}{D(\mathbf{r})} + i\frac{\omega n}{cD(\mathbf{r})}}. \tag{2.4.5}$$

In, 2.4.5 κ_0 can be also written as $\kappa_0 = \kappa_{Re} + i\kappa_{Im}$, where

$$\kappa_{Re} = \frac{1}{\sqrt{2}}\sqrt{\left(\frac{\omega^2 n^2}{D^2 c^2} + \frac{\mu_a^2}{D^2}\right)^{\frac{1}{2}} - \frac{\mu_a}{D}}, \tag{2.4.6}$$

$$\kappa_{Im} = \frac{1}{\sqrt{2}}\sqrt{\left(\frac{\omega^2 n^2}{D^2 c^2} + \frac{\mu_a^2}{D^2}\right)^{\frac{1}{2}} + \frac{\mu_a}{D}} \tag{2.4.7}$$

The complex wavenumber indicates that the wave is exponentialy attenuated and has a well defined wavelength, amplitude and phase at all points. The wavelength λ_0, the phase velocity V_p and the decay length $L_\omega$of the DPDW are defined as:

$$\lambda_0 = \frac{2}{\kappa_{Re}}, \tag{2.4.8}$$

$$V_p = \frac{\omega}{\kappa_{Im}}, \tag{2.4.9}$$

$$L_\omega = \frac{1}{\kappa_{Im}}. \tag{2.4.10}$$

As can be seen from the eq. (2.4.7), $\kappa_{Im}$is frequency dependent. For values of $\omega < 10^8$, $\kappa_{Im} \sim 1/L_d$ which means that $L_d \sim L_\omega$. In most experimental cases the modulation frequency has values in the order of 10^8 yielding a wavelength in the order of $10cm$ while the attenuation length is in the order of $1cm$. This means that the DPDWs are greatly attenuated as they propagate.

In the case of a point source and for an infinite homogeneous medium the solution of eq(2.4.4)is:

$$U_{AC}(\mathbf{r}) = \frac{S_0}{4\pi D r}\exp(i\kappa_0 r) \tag{2.4.11}$$

and therefore the frequency dependent part of the average intensity $U_{AC}(\mathbf{r}, t)$, is written as:

$$U_{AC}(\mathbf{r}, t) = \frac{S_0}{4\pi D r}\exp(i\kappa_0 r)\exp(-i\omega t) \tag{2.4.12}$$

where S_0 is the source amplitude, D is the diffusion coeficient of the turbid medium and ω is the modulation frequency.

2.4.2 Time domain

Let assume that the source is a laser pulse. For the case of an infinite medium and by applying the delta function as source term on the eq. (2.4.1):

$$S(\mathbf{r},t) = \delta(0,0) \tag{2.4.13}$$

the solution is:

$$U(\mathbf{r},t) = \frac{c}{4\pi Dct^{-3/2}} \exp\left(-\frac{r^2}{4Dct} - \mu_a ct\right) . \tag{2.4.14}$$

The pulse case can also be treated by its Fourier transform to its modulation frequencies. The transport of a pulse inside the turbid medium can be then viewed in terms of a superposition of diffuse photon-density waves, each of which propagates independently.

2.5 Boundary Conditions

The boundary conditions must also be considered for the case of non-invasive tissue measurements. In this thesis time resolved transmittance measurements are performed on diffuse slabs. The medium is irradiated by an ultrashort laser pulse and the transmitted intesity is collected by the detecting system. Therefore the expression for the boundary conditions for the slab geometry is needed in order to solve the Green's functions of the forward problem.

For the derivation of the boundary conditions two cases have to be examined. The first is when the turbid slab is in contact with an index-matching medium. The other case is like the slab-air case where an interface seperates two regions with different indices of refraction. Within the diffusion approximation the exact boundary condition for an index matched boundary is that the component of the flux normal to the interface, pointing from the non-scattering medium into the turbid medium, must be zero:

$$\mathbf{J}_{in}(\mathbf{r}) = 0 . \tag{2.5.1}$$

In the case that the turbid medium is bounded by transparent medium (like the tissue-air case) and their refractive indices are substantially different then we must consider all the possible Fresnel reflections at the interfaces from the flux inside the turbid medium. The zero-flux condition must also be considered and therefore it is assumed that all the flux traversing the interface is toward the non-diffusive medium. Thorough derivation of these boundary conditions can be found elsewhere in Refs. ([41, 42]). Generally, the boundary condition is expressed as an equation that relates the $U(\mathbf{r},t)$ with the $\mathbf{J}(\mathbf{r},t)$ in way like:

$$U(\mathbf{r},t) = \mathbf{C}\mathbf{J}(\mathbf{r},t) \cdot \hat{\mathbf{n}} , \tag{2.5.2}$$

where $\hat{\mathbf{n}}$ is the surface normal pointing outward (see Fig.1) and C is a coefficient which takes into account the refractive index mismatch [41],[42]. For the cases presented in this work C

varies from $C \sim 2$ (water/polystyrene interface) to $C \sim 5$ (water/air interface).

Generally it is difficult to obtain analytic solutions of the diffusion equation using the zero-flux requirement . A good approach is to define an extrapolated boundary at a distance z_{ex} outside the real boundary and there apply the condition $U(z_{ex}) = 0$. This extrapolation distance comes from a linear extrapolation of the fluence at the boundary to the zero-flux crossing point. A typical value for this virtual boundary is $z_{ex} = -2/(3\mu_s')$.

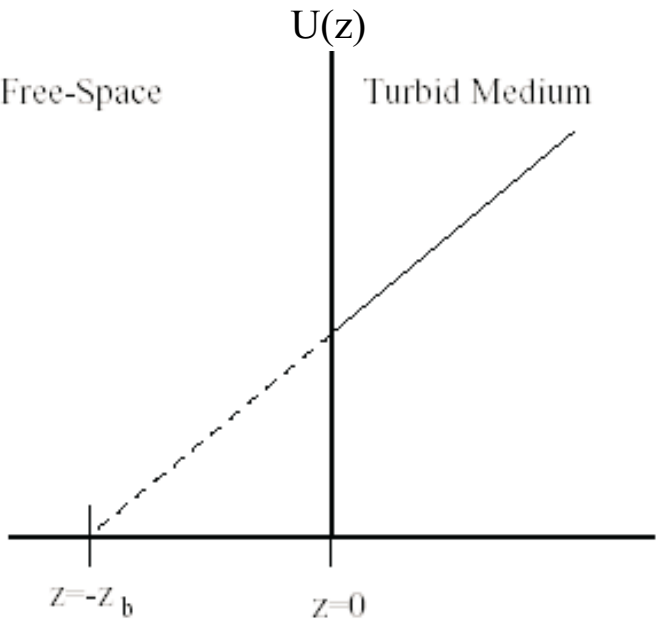

Figure 2.5.1: Schematic of the extrapolated zero boundary condition

In our approach, however, we will use the exact boundary conditions2.5.2.

2.6 Angular Spectrum Representation

The average intensity intensity $U(\mathbf{r})$ can be expressed as a superposition of plane waves by aplying the two dimensional Fourier transform. This alternative way of expressing the average intensity is called angular spectrum representation. If a complex field distribution across any plane is Fourier analyzed, the various spatial Fourier components can be identified as plane waves traveling in different directions. The field amplitude at any other point can be calculated by adding the contribution of these plane waves taking into account the phase change they have undergone in propagating to the point of interest.

Let us assume a multiple scattering medium which is source free. Any average intensity $U(\mathbf{r})$ inside the medium is a complex field distribution across a xy plane and has a two dimensional Fourier transform to K-space given by:

$$U(\mathbf{R}, z) = \int_{-\infty}^{+\infty} \widetilde{U}(\mathbf{K}, z) \exp[i\mathbf{K} \cdot \mathbf{R}] \, d\mathbf{K} \,. \tag{2.6.1}$$

while the inverse transform is given by

$$\widetilde{U}(\mathbf{K}, z) = \frac{1}{4\pi^2} \int_{-\infty}^{+\infty} U(\mathbf{R}, z) \exp[-i\mathbf{K} \cdot \mathbf{R}] \, d\mathbf{R} \,. \tag{2.6.2}$$

Suppose now that a wave is incident on the xy plane traveling in the z direction. Let the complex field across that plane at $z = 0$ be represented by $U(\mathbf{R}, 0)$. The objective is to calculate the consequent field at plane z ($U(\mathbf{R}, z)$). If in eq. (2.4.4) the $U(\mathbf{r})$ is substituted with the eq. (2.6.2), one obtains:

$$\frac{\partial^2 \widetilde{U}(\mathbf{K}, z)}{\partial z^2} + \left(\kappa_0^2 - |\mathbf{K}|^2\right) \widetilde{U}(\mathbf{K}, z) = 0 \tag{2.6.3}$$

The solution to eq. (2.6.3) is:

$$\widetilde{U}(\mathbf{K}, z) = A(\mathbf{K}) \exp[iq(\mathbf{K}) z] \,, \tag{2.6.4}$$

where:

$$q(\mathbf{K}) = \sqrt{\kappa_0^2 - |\mathbf{K}|^2} \,. \tag{2.6.5}$$

Therefore the effect of propagation over a distance z is simply a change in the relative phases and amplitudes of the various components of the angular spectrum. The spatial frequency filter:

$$F(\mathbf{K}, z) = \exp[iq(\mathbf{K}, z)] \,, \tag{2.6.6}$$

constitutes the propagation transfer function. It should be mentioned that since q always has a complex part, $F(\mathbf{K}, z)$ decays exponentially with z.

The scattered wave $U(\mathbf{r})$ it is expressed by its angular spectrum representation of plane waves, by a superposition of such waves of amplitude $A(\mathbf{K})$ and wave vector $\mathbf{k} = (\mathbf{K}, q)$, with $|k| = \kappa_0$ as:

$$U(\mathbf{R}, z) = \int_{-\infty}^{+\infty} A(\mathbf{K}) \exp[i\mathbf{K} \cdot \mathbf{R} + iq(\mathbf{K}) z] \, d\mathbf{K} \,. \tag{2.6.7}$$

Therefore the effect of propagation over a distance z is simply a change in the relative phases and amplitudes of the various components of the angular spectrum.

2.7 Limits of the Diffusion Approximation

Many research papers are devoted to explore the range of validity of the diffusion approximation [17, 18, 34, 43, 44, 45, 46, 47, 48, 49, 23, 24, 25]. When dealing with length scales in the order of l_{tr} the measured intensities strongly deviate from the ones predicted by the standard diffusion equation. This has commonly been attributed to a failure of the diffusion approximation and it is believed that the diffusion approximation furnishes accurate results only for large length and time scales, where light has suffered multiple scattering events and can thus be treated as diffusive [45].

Chapter 3

Improving the Diffusion Approximation

According to the conclusions of the previous chapter, diffusion theory is correctly applied for system lengths in the order of 10 transport mean free paths. Diffusion theory assumes that the light inside the medium is diffusive which means that the light propagates almost isotropically. This means that for slabs of thickness in the order of few mean free paths, the predictions of diffusion theory will break down. In this chapter the diffusion equation will be improved expanding its validity without losing much of its simplicity. The approach that it will presented concerns improvements on the approximations used through the derivation of the diffusion equation.

Four main contributions are introduced in order to correctly model the problem of a laser pulse incident to a diffusive slab of few mean free paths. These consist on:

A) a frequency-dependent diffusion coefficient

B) a frequency-dependent zero-flux boundary condition

C) an exponentially decaying source

D) the contribution of non-scattered light

These contributions are described in detail and are finally implemented in the expression for a slab.

The theoretical approach used throughout this chapter is always to Fourier-transform to the frequency-domain and then Fourier-transform to K-space to solve exactly for the boundary conditions. All time-dependent solutions are subsequently retrieved in real space and time by Fourier inversion.

We shall consider the case depicted in Fig. 3.0.1, where we have a slab of thickness L, with optical properties defined by an absorption coefficient μ_a, a reduced scattering coefficient μ_s' and an index of refraction n_0. In the following we will be interested on the transmitted and

reflected intensity from the slab, due to a source impinging from a non-scattering medium with index of refraction n_{in} located to the left of the scattering medium.

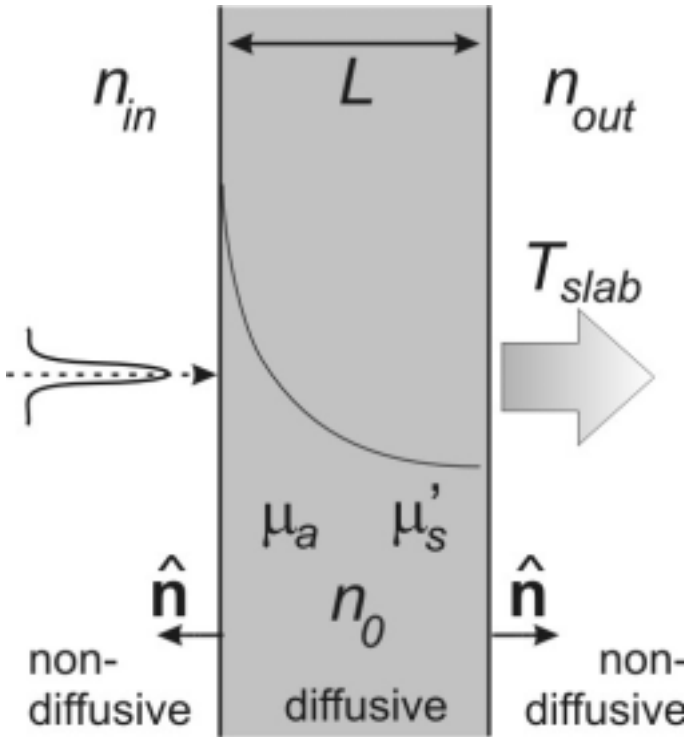

Figure 3.0.1: Scattering geometry for a slab of width L.

3.1 Dynamic Diffusion Coefficient

This section will deal with the eq. (2.2.3) and the approximations taken on section 2.3. In section 2.3 we assumed that the variations in the diffuse total flux take place over a time scale much larger than the lapse between scattering events on particles of the medium and also that the time of change of the total flux due to absorption is much larger than the time between scattering events. With these assumptions the term $(\partial/\partial t + \mu_a c/n)$was neglected and eq. (2.2.3) reduced to the well known Fick's law which is an expression for the steady state. Even when the source is time-dependent, Fick's law is a good approximation for biological tissues if the source frequencies are less than $\sim 1GHz$.

From Eq. (2.2.9) a constant diffusion equation was introduced which means that photon diffusion takes place instantly. The diffusion coefficient is a parameter that characterizes the rate of spread, which can be time dependent. The standard diffusion equation [eq. (2.4.1)] with a constant diffusion coefficient is the simplest way to describe phenomena of light energy propagation. Actually, the diffusion process is more complicated than that described by the diffusion equation, mainly because in the case of a laser source, applied from outside the slab,

the photons are injected with velocity along a direction and need some time for the light to be considered as diffusive. The diffusion coefficient in this process should be thus considered as time-dependent.

In order to derive a frequency(or time)-dependent diffusion coefficient we shall briefly reproduce the derivation of Fick's Law. If instead of approximating Eq. (2.2.3) we consider the case in which the average intensity U is modulated at a frequency ω, in which case the temporal dependence of U_t and $\mathbf{J}_t$ is defined as: $U_t(\mathbf{r},t) = U(\mathbf{r})\exp[-\omega t]$ and $\mathbf{J}_t(\mathbf{r},t) = \mathbf{J}(\mathbf{r})\exp[-\omega t]$. By inserting the frequency dependent expressions for the U_t and $\mathbf{J}_t$ in Eq. (2.2.3) we have:

$$\nabla U(\mathbf{r},\omega) = -3\left(\mu_s' + a\mu_a - i\frac{\omega n_0}{c}\right)\mathbf{J}(\mathbf{r},\omega) \tag{3.1.1}$$

Comparing this expression with the Fick's law (Eq. (2.2.8))a frequency-dependent diffusion coefficient is defined as:

$$\widetilde{D}(\omega) = \frac{1}{1 - i\omega t_{tr}}D \tag{3.1.2}$$

where t_{tr} is the average time required for light to travel a transport mean free path, defined in the presence of absorption as $t_{tr} = n_0/[c(\mu_s' + a\mu_a)]$. An expression equivalent to Eq. (3.1.2) was presented in Refs. [50] and [51]. The shape of $\widetilde{D}$ is shown in Fig. 3.1.1 for the $\mu_a = 0.02\,cm^{-1}$, $\mu_s' = 10cm^{-1}$ case, together with its time-domain D_t shape. From Eq. (3.1.2) and Fig. 3.1.1, we see that the diffusion coefficient is practically frequency independent up to $\omega \sim 10GHz$. A thorough study of the resulting diffusion equation when using Eq. (3.1.2) versus that obtained by the standard diffusion equation Eq. (2.2.10) can be found in Ref. [51], where it is shown that at high modulation frequencies Eq. (3.1.2) furnishes better results than Eq (2.2.10). By using Eq. (3.1.2), Fick's law can be rewritten in time- domain as a convolution:

$$\mathbf{J}(\mathbf{r},t) = -D(t-t') * \nabla U(\mathbf{r},t') \tag{3.1.3}$$

Since $\langle D\rangle = D$ for long times the time-dependent diffusion coefficient D_t can be approximated to $D_t(t-t') \approx D\delta(t-t')$ (inset of Fig. 3.1.1), which introduced in Eq. (3.1.3) gives us the classical expression of Fick's law. It is well known [43] that one of the main drawbacks of the diffusion approximation is that it assumes that diffusion takes place instantly. As we will show in the following sections, this breakdown of the diffusion approximation for short times can be alleviated by considering a dynamic diffusion coefficient. Similar conclusions were drawn in Refs. [18, 24], where it is presented a more elaborate derivation of a time-dependent diffusion coefficient.

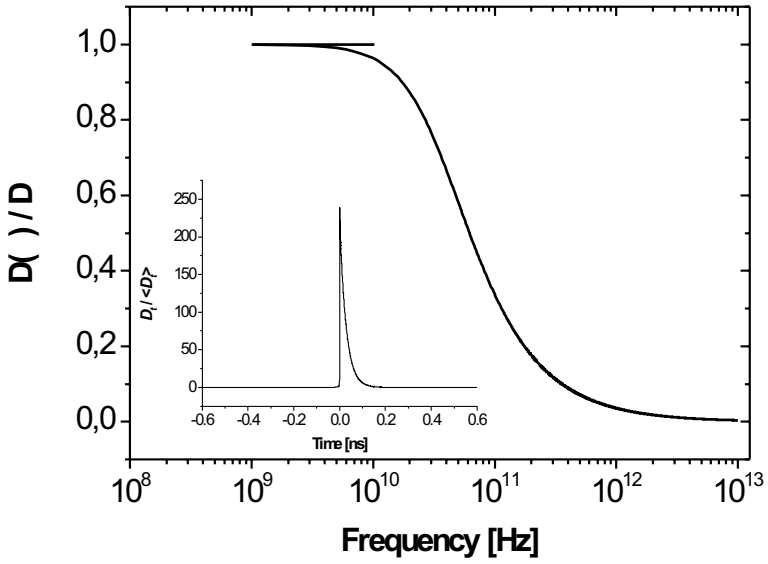

Figure 3.1.1: Normalized diffusion coefficient versus frequency for the $\mu_a = 0.02\,cm^{-1}$, $\mu_s' = 10\,cm^{-1}$case. Inset: Normalized diffusion coefficient versus time in nanoseconds. Absolute values $|D(\omega)|/D$, $|D_t|/\langle D_t \rangle$, represented in both cases.

3.2 Zero-flux Boundary Condition

Once we have defined a frequency-dependent diffusion coefficient [see Eq. (3.1.2)], we shall use this expression in the boundary condition for diffusive/non-diffusive interfaces. By using Eq. (3.1.2), the frequency-dependent boundary condition for diffusive/non-diffusive interfaces is:

$$U_\omega(\mathbf{r},\omega) = -C\widehat{D}(\omega)\frac{\partial U_\omega(\mathbf{r},\omega)}{\partial \hat{\mathbf{n}}}\,. \tag{3.2.1}$$

The difference between Eq. (3.5.1) and the standard Robin boundary condition [eq. (2.5.2)] is easily understood in terms of the extrapolated distance $l_{ext} = CD$. Within the standard formulation l_{ext} is a constant, however, Eq. (3.5.1) implies that the extrapolated distance is a dynamic quantity that decreases for high frequencies proportionally to what is shown in Fig. 3.1.1. Thus, by applying a frequency dependent diffusion corfficients the boundary condition became frequency dependent.

3.3 Exponentially decaying source

As it was seen in sections 2.41 and 2.4.2 the most common way of defining the source within a scattering medium is to consider a point source located at $z \sim l_{tr}$ inside the medium. This delta

function implies isotropic emission of light. This approach to the source term may seem like an overly simplistic approximation and has been shown to provide very good results for large source/detector distances in phantom and in-vivo experiments [2, 9, 29, 32]. However for any real situation when a sample is illuminated by a laser pulse of finite width a clearly anisotropic intensity distribution is generated. For short source/detector distances more elaborate methods have been presented to model the delivery of light into the highly scattering system. One of such models considers that the incident source is a collection of point sources with exponentially decaying intensities as we go deeper into the medium [50]. The expression for the incident source is obtained directly from the Radiative Transfer Equation (see Ref. [7], Ch. 9), considering that in weakly scattering media the equation to solve is:

$$\frac{n_0}{c}\frac{\partial I\left(\mathbf{r},\hat{\mathbf{s}},t\right)}{\partial t}+\hat{\mathbf{s}}\cdot\nabla I\left(\mathbf{r},\hat{\mathbf{s}},t\right)+\left(\mu_a+\mu_s'\right)I\left(\mathbf{r},\hat{\mathbf{s}},t\right)=I_0\left(\mathbf{r},\hat{\mathbf{s}},t\right)\ . \tag{3.3.1}$$

where I_0 is the incident intensity at the boundary and $\mathbf{r}=(\mathbf{R},z)$. For a plane interface at $z=0$, the specific intensity due to a flux at $\mathbf{R}=0$, $z=0$ in the frequency domain is derived from Eq. (3.3.1) as:

$$I\left(z,\hat{\mathbf{u}}_z,\omega\right)=I_0\left(\mathbf{R}=0,z=0\right)\exp\left[\left(-\left(\mu_a+\mu_s'\right)+i\frac{\omega n_0}{c}\right)z\right]\ . \tag{3.3.2}$$

Since the power generated per unit volume E within the diffusive medium is defined as the solid angle integral of Eq. (3.3.3), we obtain for the source term:

$$E\left(\mathbf{r}\right)=E_0\exp\left[\left(-\left(\mu_a+\mu_s'\right)+i\frac{\omega n_0}{c}\right)z\right]\delta\left(\mathbf{R}\right)\ . \tag{3.3.3}$$

In the plane-wave case Eq. (3.3.3) reduces to $E\left(z\right)=E_0\exp\left[\left(-\left(\mu_a+\mu_s'\right)+i\omega n_0/c\right)z\right]$, which is the case presented in Ref. [50]. Given the power generated per unit volume E, the diffuse intensity generated within the scattering medium is given by:

$$U^{(inc)}\left(\mathbf{r}\right)=\frac{1}{4\pi}\int_V E\left(\mathbf{r}'\right)g\left(\mathbf{r},\mathbf{r}'\right)d\mathbf{r}' \tag{3.3.4}$$

where g is the infinite homogeneous Green function. Eq. (3.3.4) can be solved in a closed form in K-space by using the expression for the Green function [52, 53, 54, 55, 56, 57] :

$$g\left(\mathbf{K},z\right)=\frac{i}{2\pi q\left(\mathbf{K}\right)}\exp\left[iq\left(\mathbf{K}\right)z\right] \tag{3.3.5}$$

where $q=\sqrt{\kappa_0^2-\mathbf{K}^2}$, being κ_0 the complex wavenumber [51, 40] for a frequency-dependent diffusion coefficient [50, 51] (defined in section 2.4.1). For the case of a slab of width L the incident diffuse intensity is given by Eq (3.3.4) when applying to it the eqs. (3.3.3) and (3.3.5):

$$\widetilde{U}^{(inc)} = \frac{E_o}{4\pi}\int_0^L \exp\left[-\overline{\mu}z\right]\frac{i}{2\pi q\left(\mathbf{K}\right)}\exp\left[iq\left(\mathbf{K}\right)z\right]dz \tag{3.3.6}$$

which can be exactly solved as:

$$\widetilde{U}^{(inc)} = \frac{E_o}{4\pi}\frac{i}{2\pi q\left(\mathbf{K}\right)}\left\{\frac{\exp\left[iq\left(\mathbf{K}\right)z\right]-\exp\left[-\overline{\mu}z\right]}{\overline{\mu}+iq\left(\mathbf{K}\right)z}+\frac{\exp\left[-\overline{\mu}z\right]-\exp\left[-\overline{\mu}z\right]\exp\left[iq\left(\mathbf{K}\right)z\left(L-z\right)\right]}{\overline{\mu}-iq\left(\mathbf{K}\right)z}\right\} \tag{3.3.7}$$

where

$$\overline{\mu} = \mu_a + \mu_s' - \frac{\omega n_0}{c}\,. \tag{3.3.8}$$

Eq. (3.3.7) will be used in deriving an analytical solution for a slab. It has to be mentioned that this expression still does not include the boundary conditions, it only considers light contribution from inside the slab $[0, L]$. The time-dependent version in real space of Eq. (3.3.7) can be readily obtained through Fourier inversion:

$$U^{(inc)}\left(\mathbf{r},t\right) = \int_{-\infty}^{-\infty}\exp\left[-i\omega t\right]d\omega\int_{-\infty}^{-\infty}d\mathbf{K}\widetilde{U}^{(inc)}\left(\mathbf{K},z,\omega\right)\exp\left[i\mathbf{K}\cdot\mathbf{R}\right]\,. \tag{3.3.9}$$

As stated earlier, the approach is to Fourier-transform to the frequency-domain and then Fourier-transform to K-space to solve exactly for the boundary conditions of Eq. (3.5.1). All time-dependent solutions are retrieved in real space and time by using the inverse transformation of eq. (3.3.9).

3.4 Ballistic Contribution

In order to account for light that has not suffered multiple scattering and is thus not diffusive we consider the simplistic approximation that there is a partition of energy between the diffusive and non-diffusive signal as:

$$U_{total}\left(\mathbf{R},t\right) = \left(1-A\right)U_{dif}\left(\mathbf{R},t\right) + AI_0 \tag{3.4.1}$$

$$\widetilde{U}_{total}\left(\mathbf{K},t\right) = \left(1-\widetilde{A}\right)\widetilde{U}_{dif}\left(\mathbf{K},t\right) + \widetilde{A}\widetilde{I}_0 \tag{3.4.2}$$

where A and $\widetilde{A}$ indicate how much of the incident energy is ballistic in the time and frequency domains, respectively, while $I_0$and $\widetilde{I}_0$ are cinstants in units of $J/cm^2$and W/cm^2, respectively and magnitud 1. This expression is derived from Eqs. (3.3.2)-(3.3.4), by assuming that $(1-A)$ of the incident intensity I_0 is converted into diffusive light. For the case where cross-polarized measurements are taken, $A = 0$.

This work considers the most general case of depolarized incident light. At this point it

should be stated that the value of A obtained during the fittings presented in Chapter 5 did not affect strongly the value of the retrieved reduced scattering coefficient, but played a crucial role for thicknesses $L < 3t_{tr}$ basically contributing to improving the shape of the fit in the time-domain. A more elaborate and accurate model than Eqs. (3.4.1), (3.4.2) has been presented in Ref. [18]. However, since this model has been derived in the time-domain, deriving the expression for a slab with the correct boundary conditions [see Eq. (3.5.1)], and by including an exponentially decaying source [Eq. (3.3.7)] would result in a time-consuming operation. The method of images could be used in this case, but as will be shown in Chapter 5 is not appropriate for thin samples.

3.5 Expression for a Slab

For the derivation of the exact and general solution for a slab the procedure followed is presented in Ref. [58]. Only the most relevant steps of this approach, will be shown here.

Eq. (3.3.7) in section 3.3 gives the diffuse intensity generated within the scattering medium due to an exponentially decaying source and is referred as the incident diffuse intensity. This intensity was found in K-space for a given modulation frequency ω. In order to derive an expression for the slab the boundary conditions should be included.

By using the zero flux condition presented in section 3.2:

$$U_\omega(\mathbf{r},\omega) = -C\widehat{D}(\omega)\frac{\partial U_\omega(\mathbf{r},\omega)}{\partial \hat{\mathbf{n}}}. \tag{3.5.1}$$

and the expression for the Fick's Law in its angular spectrum representation:

$$\tilde{J}_n(\mathbf{K},z) = -D\frac{\partial \widetilde{U}(\mathbf{K},z)}{\partial z}$$

then the expressions for the reflection R and transmittance T coefficients are derived in the case of a diffusive/non-diffusive interface [58]:

$$R_{in,out}(\mathbf{K}) = \frac{iC_{in,out}\widetilde{D}(\omega)\,q(\mathbf{K})+1}{iC_{in,out}\widetilde{D}(\omega)\,q(\mathbf{K})-1} \tag{3.5.2}$$

$$T_{in,out}(\mathbf{K}) = \frac{2iC_{in,out}\widetilde{D}(\omega)\,q(\mathbf{K})}{iC_{in,out}\widetilde{D}(\omega)\,q(\mathbf{K})-1} \tag{3.5.3}$$

where the subindex in, out denotes when the boundary condition coefficient C is considered from the left (reflection) or the right (transmittance) (see Fig. 3.0.1). Equivalent expressions for a diffusive/diffusive interface are derived in Ref. [59].

With the aid of the above coefficients we can treat the slab as a "fabry-parot" for the diffuse waves as they experience multiple reflections at the slab's interfaces. By following the steps

presented in Ref. [58], and using the fact that the flux that exits the slab is given by Eq. (2.5.2), we reach the expression for transmittance ($z = L$):

$$\widetilde{T}_{slab}(\mathbf{K},\omega) = \frac{1}{C_{out}} \frac{\widetilde{U}^{(inc)}(\mathbf{K}, z = L) + R_{in}(\mathbf{K}) \exp[iq(\mathbf{K})L]\, \widetilde{U}^{(inc)}(\mathbf{K}, z = 0)}{1 - R_{in}(\mathbf{K}) R_{out}(\mathbf{K}) \exp[2iq(\mathbf{K})L]} T_{out}(\mathbf{K}) \quad (3.5.4)$$

and reflection ($z = 0$):

$$\widetilde{R}_{slab}(\mathbf{K},\omega) = \frac{1}{C_{in}} \frac{\widetilde{U}^{(inc)}(\mathbf{K}, z = 0) + R_{out}(\mathbf{K}) \exp[iq(\mathbf{K})L]\, \widetilde{U}^{(inc)}(\mathbf{K}, z = L)}{1 - R_{in}(\mathbf{K}) R_{out}(\mathbf{K}) \exp[2iq(\mathbf{K})L]} T_{in}(\mathbf{K}) \quad (3.5.5)$$

where $\widetilde{U}^{(inc)}$is defined in Eq. (3.3.7). Eqs. (3.5.4) and (3.5.5) represent the analytical expression for the spatial and temporal distribution of light reflected and transmitted from a slab of width L. The denominator $1 - R_{in}R_{out}exp[2iqL]$ takes intoaccount the multiple reflections between the interfaces of the slab.

In the case when we are interested in the total transmitted/reflected intensity, we may use the following property of Fourier-transforms:

$$\widetilde{T}^{total}_{slab}(\omega) = \int_{-\infty}^{+\infty} \widetilde{T}_{slab}(\mathbf{R},\omega)\, d\mathbf{R} = \widetilde{T}_{slab}(\mathbf{K} = 0,\omega)\ . \quad (3.5.6)$$

In this case, the total reflection and transmittance for a slab can be easily found in the time-domain by using Eqs. (3.5.4) and (3.5.5) as:

$$T^{total}_{slab}(t) = \int_{-\infty}^{-\infty} \widetilde{T}_{skab}(\mathbf{K} = 0,\omega) \exp[-i\omega t]\, d\omega \quad (3.5.7)$$

$$R^{total}_{slab}(t) = \int_{-\infty}^{-\infty} \widetilde{R}_{slab}(\mathbf{K} = 0,\omega) \exp[-i\omega t]\, d\omega\ . \quad (3.5.8)$$

All the results presented in the following section were fitted for the total transmittance using Eqs. (3.5.7).

Chapter 4

Experimental Methods

This chapter describes the techniques used in this work for performing time resolved measurements on tubid media. Measurements were performed on Intralipid phantoms, on breast biopsies and on Monte Carlo simulations of high scattering media. In each case the sample had the slab geometry. Experimental data from the above experiments are used in order to fit analytic expressions derived from the theoretical models. The Monte Carlo data and the phantom samples are used for validation theory since their optical properties are well known. On the other hand, biopsy measurements were performed for tissue characterization.

While time resolved measurements are commonly performed to characterize scattering media, it is not the only approach. Both continuous wave and frequency modulated sources can be fed inside the medium. So far, it is not clear which experimental approach is better. The criterion of such a choice is mostly dependent of the information that a technique can provide together with its simplicity. For a source-detector pair, the pulsed-time approach clearly carries more information, as a result of the many frequency components.

4.1 Experimental

In general, time resolved measurements concern the irradiation of a medium with a laser pulse and the detection of either the transmitted or the reflected signal. In this work, only transmittance measurements were performed because transmittance contains higher info on tissue average properties, since the main component travels longer distances than in reflection mode. Moreover reflection measurements have a more complicated experimental configuration with the use of fibers as signal collectors.

4.1.1 Experimental setup

The setup used in the experiments is typical for time resoved transmittance measurements and is shown in Fig. (4.1.1). Before describing the different configurations for the tagerts irradiated it is useful to examine the laser source, the detecting system and the rest experimental setup.

Laser source

The laser source was an ultra fast pulsed mode-locked Ti:Sapphire laser emitting $200\,fs$ pulses at $830\,nm$. The laser was pumped by a diode pumped, frequency doubled Nd:YAG laser operating with a power of $5\,Watt$. The repetition rate of the Ti:Sapphire was $82\,MHz$ with an average power of $\sim 1\,Watt$. The laser beam is guided with the use of optics into the sample so that the incident beam enters the slab perpendicularly. The diameter of the beam at the sample was controlled with an iris to be $\sim 3mm$ being the samples irradiated with a power of $\sim 100\,mW$.

Streak Camera

The system used to detect the transmitted intensity consisted of a Hamamatsu C5680 Streak Camera and a high sensitivity CCD camera. In order to collect the total transmitted light, a lens was placed between the sample and the slit of the streak camera. The distances between the sample, the lens and the slit are adjusted so that the lens can deliver an 1:1 image of the back boundary of the sample to the slit.

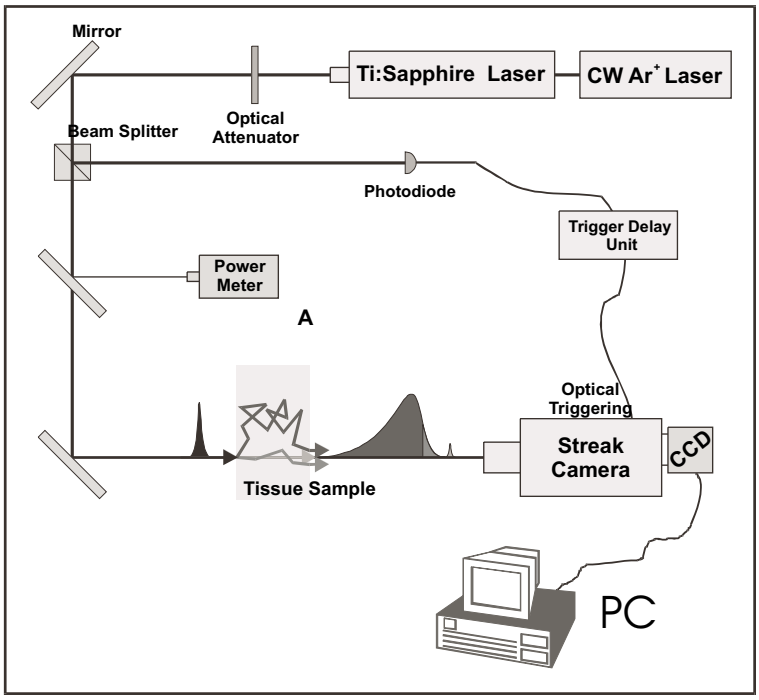

Figure 4.1.1: Experimental setup for time resolved transmission measurements

Although it is called a "camera", a streak camera is quite different from the video cameras and still cameras that we load with film to take pictures of the people and objects around us. The Streak Camera is a device to measure ultra-fast light phenomena and delivers intensity vs. time vs. position(or wavelength) information. It's name dates back to the early days of the high speed rotating cameras. These cameras would "streak" reflected light onto film. No other imstruments which directly detect ultra-fast phenomena have better temporal resolution than the streak camera. Used in combination with proper optics, it is possible to measure time variation of the incident light with respect to position (time and space resolved measurements). Streak Camera has a maximum temporal resolution of $2ps$ and can handle anything from single event phenomena to high-repetition phenomena in the GHz range.

Fig. (4.1.2) shows the operating principle of the streak camera. The light being measured passes through a slit and is formed by the optics into a slit image on the photocathode of the streak tube. Let's assume at this point, four optical pulses which vary very slightly in terms of both time and space, and which have different optical intensities, are input through the slit and arrive at the photocathode. The incident light on the photocathode is converted into a number of electrons proportional to the intensity of the light, so that these four optical pulses are converted sequentialy into electrons. They then pass through a pair of accelerating electrodes, where they accelerated and bombarded against a phosphor screen.

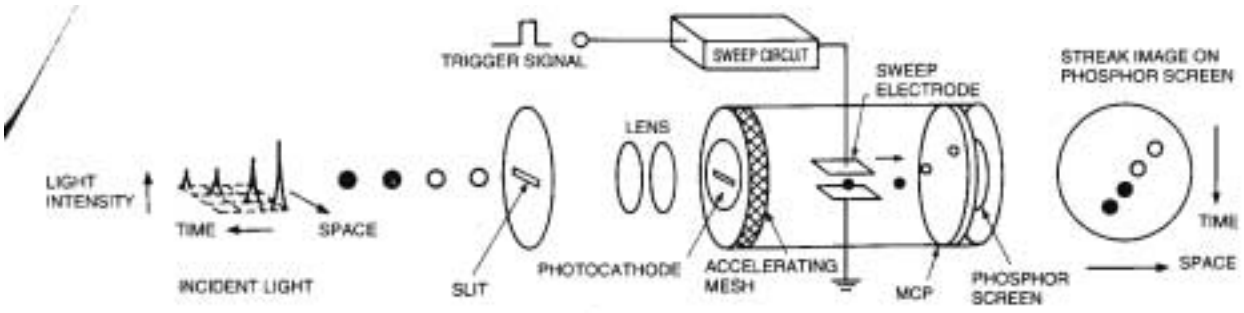

Figure 4.1.2: Operating principle of the Streak Tube

As the electrons produced from the four optical pulses pass between a pair of sweep electrodes, high voltage is applied to the sweep electrodes at a timing synchronized to the incident light (see Fig. 4.1.3). This initiates a high-speed sweep (the electrons are swept from top to bottom). During the high-speed sweep, the electrons, which arrive at slightly different times, are deflected in slightly different angles in the vertical direction, and enter the MCP (micro-channel plate).

As the electrons pass the MCP, they are multiplied several thousands of times, after which they impact against the phosphor screen, where they are converted again into light. On the phosphor screen, the phosphor image corresponding to the optical pulse which was the earliest to arrive is placed in the uppermost position, with the other images being arranged in sequential

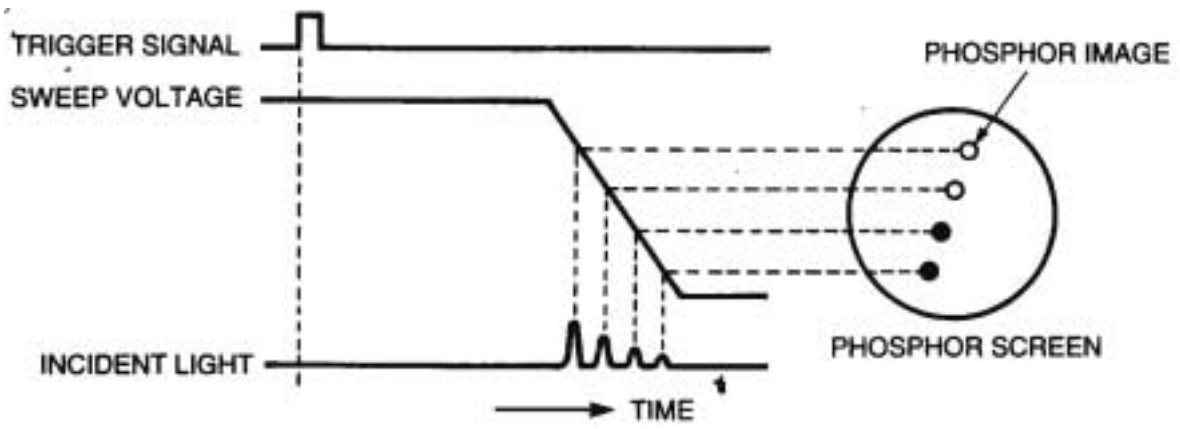

Figure 4.1.3: Operation timing at the time of the sweep

order from top to bottom: in other words, the vertical direction on the phosphor screen serves as the time axis. Also, the brightness of the various phosphor images is propotional to the intensity of the respective incident optical pulses. The position in the horizontal direction of the phosphor image corresponds to the horizontal location of the incident light.

In this way the streak camera can be used to convert changes in the temporal and spatial intensity of the light being measured into an image showing the brightness distribution on the phosphor screen. We can thus find the optical intensity from the phosphor image, and the time and incident position from the location of the phosphor image.

The mode-locked Ti:Sapphire laser which was used, was combined with Synchroscan unit (Hamamatsu M5675), which is manufactured to be synchronized with the mode locking $82\,MHz$ frequency of this laser. This unit could operate in four different sweep speeds covering temporal ranges from $200\,ps$ to $2\,ns$ and the temporal resolution that can be accomplished was $\leq 2\,ns$.

In order to measure ultra-high speed optical phenomena using a streak camera, a trigger section and a readout section are required. The basic configuration of this system is shown in Fig.(4.1.4). The trigger section controls the timing of the streak sweep. This section has to be adjusted so that a streak sweep is initiated when light being measured arrives at the streak camera. For this purpose, a delay untit is used, which controls how long the trigger signal which initiates the streak sweep is delayed. In the experiments presented here, the Hamamatsu C1097-01 trigger was used enabling delay times from $30\,ps$ to $31.96\,ns$. The trigger signal is produced when a thin glass "steals" a small portion of the incident beam sending it to to the p-i-n photodiode (also shown in Fig. (4.1.4)).

The readout section reads and analyzes sreak images produced on the phosphor screen, which is on the output side of the streak camera. Because the streak image is faint and disappears in an instant, a high-sensitivity Hamamtsu C4880 CCD camera is used that detects images of the phosphor screen. The CCD camera is cooled by a thermoelectric device employing a

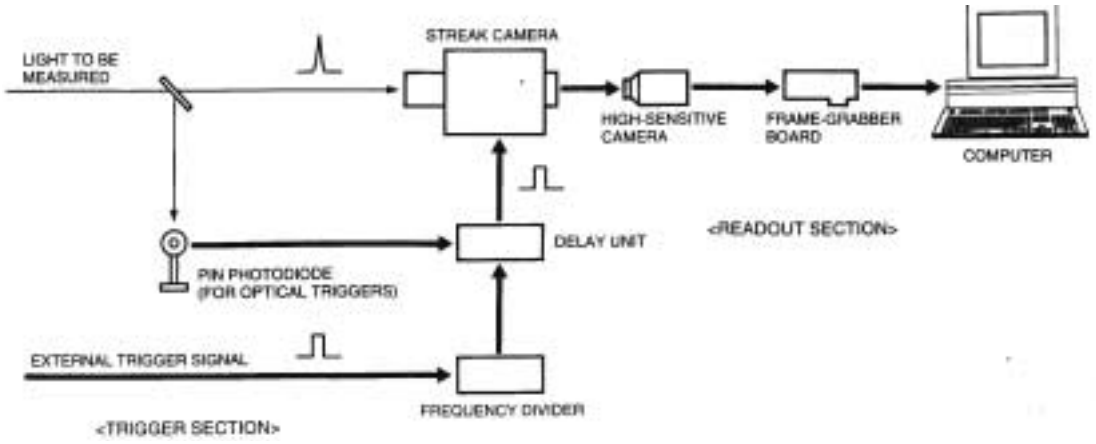

Figure 4.1.4: Basic system configuration of the Streak Camera

Peltier cooler, which enables temperatures down to $-50\,^oC$, thus reducing the dark current and achieving better signal to noise (S/N) ratios. The dynamic range of the CCD is defined as the ratio of the saturation charge volume to the readout noise, being $1:5000$.

Analysis of streak images is done by transferring the images through a frame grabber board to a computer. The system used was the HPD-TA (Temporal Analyzer) which is a high-performance digital data acquisition and control system specifically designed to read out images from the Hamamatsu streak camera's phosphor screen. For better image quality the background accounting for the electronic noise (dark current), the temperature of the photocathode or the leaks from the optics, was subtracted after acquisition of each image, keeping all the settings the same. A Streak Camera image is presented in Fig.(4.1.5). The image shown in Fig.(4.1.5) is the transmitted pulse through a 2mm scattering sample. Having in mind that the vertical axis represents time and that the pseudocolors are analogous to the Intensity variations, the temporal profile of the Streak Image has the shape of Fig. (4.1.5 b). Similar temporal profiles has been recorded throughout this work from different types of samples in order to retrieve the optical parameters.

4.2 Samples

As already mentioned in the introduction of this chapter both Inralipid and biopsy samples were irradiated with the experimental setup of figure (4.1.1).

4.2.1 Tissue phantoms

Tissue phantoms are used for validating models of light propagation. A tissue phantom should mimic the optical properties of tissue in terms of scattering coefficient, anisotropy factor, absorption coefficient and refractive index. An ideal phantom should be easy to create and to

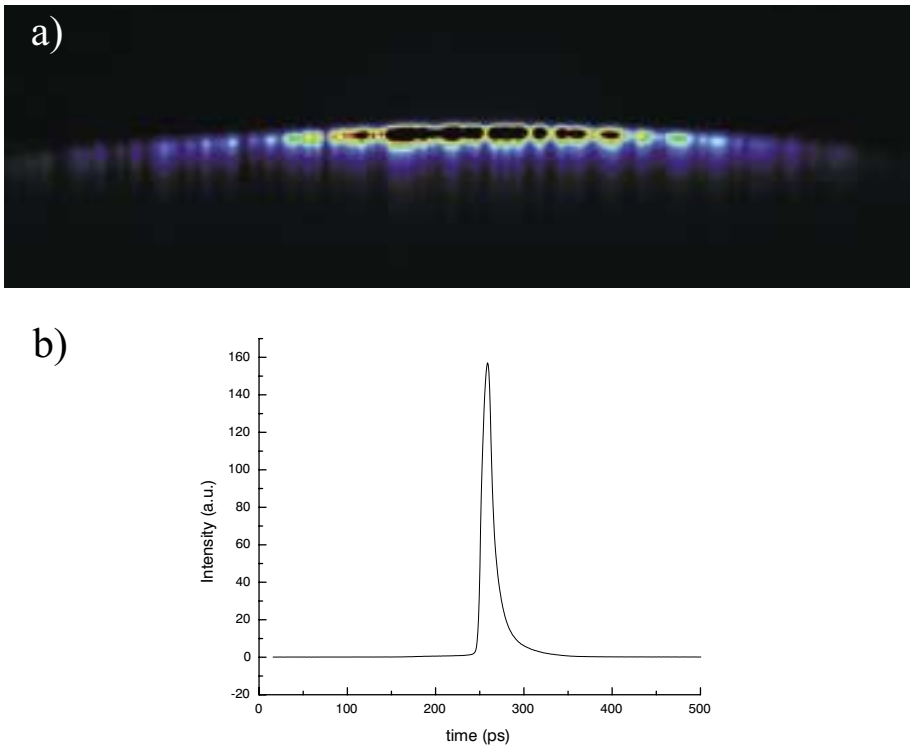

Figure 4.1.5: a) Characteristic image recorded with the Streak Camera. It corresponds to the transmitted pulse from a 2mm scattering sample b) Temporal profile of the Streak Image shown in a)

control its shape. Intralipid is a scattering material that has been adopted by the biomedical community. It is the basis of the phantoms been made during this work. As an alternative scattering material, resins like polyester are oftenly used.

Phantoms used in this work are made of Intralipid and water. Intralipid is an emulsion of water and soy bean fat used for intravenous feeding of hospitaized patients. It is a polydisperse suspension of particles with an average diameter of $\sim 0.4\mu m$, but a relatively wide range of sizes (i.e. from $\sim 0.1\,\mu m$ to $\sim 1.1\,\mu m$). Many studies have been performed on the optical properties of Intralipid [60, 61, 62].

The Intralipid phantoms can be used either in its liquid form, but also solid by adding a hardener to the solution. In the measurements performed here, solid phantoms were used. The phantom was placed inside a transparent polystyrene petri-dish and then on a XY translation stage enabling measurements for different source positions. The petri-dish was placed so that the phantom slab was bounded in the back side by the PMMA of the dish while the front side was in free contact with the air.

4.2.2 Biopsy samples

Female breast biopsy samples from a total of 27 patients have been measured with ages ranging from 35 to 80 years old. The tissue samples were obtained from tumor excision or biopsy operations performed at the Department of Surgerical Oncology of the University Hospital of Heraklio. The samples, which were finally irradiated, were provided, being properly cut, by the Department of Pathology of the University Hospital.

The samples were categorized as fat, normal glandular and tumor tissue and their thickness was typical for biopsies i.e. varied from 0.5 to 3.0 mm. All samples were formally processed and histologically analyzed at the end of our measurements. Usually, biopsy samples have arbitary shape. In order to obtain the appropiate geometry, they were placed between two transparent PMMA slabs being to conform a slab geometry Fig. 4.2.1. The distance of these two PMMA slabs can be adjusted by micrometer screws so that the thickness of the sample is known at a micrometer accuracy. Knowledge of the exact thickness of phantoms is important for tissue characterization, since theory is sensitive to small variations of thickness.

Figure 4.2.1: Sample holder with micrometer screws for thickness adjustment

Similar to the case of phantom samples the biopsy holder was placed on a XY translation stage enabling measurements on different parts of the biopsy, so that scaning can be performed. As it was mentioned, in this configuration both boundaries of the tissue are in contact with the PMMA. All tissue measurements performed at room temperature.

4.2.3 Monte Carlo solutions

In addition to experimental measurements we also used Monte Carlo simulations to assess the accuracy of our analytical expressions eqs. (3.5.7) (3.5.8). A detailed description of the Monte Carlo method for light propagation in scattering media is described in Refs. [13, 14] and references therein.

Monte Carlo simulations of photon propagation offer a flexible yet rigorous approach toward photon transport in turbid tissues with a signal-to-noise ratio and boundary conditions that are impossible to achieve in the laboratory. Monte Carlo as a technique provides full numerical solutions to the RTE in contrary to the analytic expressions that we obtain from the diffusion equation. The results, therefore, are expressed as histograms of photons and not as analytic expressions of a time dependent intensity.

The method relies on simulating the trajectories of a large number of photons launched in a tissue-like medium. The rules of photon propagation are expressed as probability distributions that describe the step size of photon movement between sites of photon-tissue interaction, and the angles of deflection in a photon's trajectory when a scattering event occurs. The simulation is rigorous and can be applied to solve a variety of problems without any limitations. However, the method is statistical in nature on calculating the propagation of a large number of photons by the computer. As a result, this method requires a large amount of computation time.

To briefly describe the approach used, packets of photons are injected orthogonally into the tissue the one after the other. Each photon packet is initially assigned a weight, W, equal to unity. The step size of the photon packet is calculated based on a sampling of the probability distribution for photon's mean free path μ_t. Once the step size is specified the packet is moved in the tissue to an interaction site. As the photon takes a step some attenuation of the photon weight by the interaction site is calculated. The amount of weight lost due to this interaction is determined by the absorption coefficient. Once the photon packet has been moved and its weight decremented, it is ready to be scattered. The probability distribution for the cosine of the scattered angle is described by the well known Henyey Greenstein formula for tissue scattering. The same process is repeated continuously untill the packet hits a boundary. From the Fresnel's formulas, a probability is computed for the reflection or not of the photon packet depending of its angle of incidence. If the photon is internally reflected it continues to wonder inside the medium. On the other hand, if it escapes the tissue at a certain point from either side, it ads its weight to the total reflection or transmittance at this certain point. A photon can be absorbed inside the tissue if its weight has been decreased after multiple scattering to a value less than a defined threshold.

The number of photons required depends largely on the the problem, the accuracy needed and the spatially resolution desired. For example, in the case of computing the total reflection from a semi-infinite medium, only about 5000 photons may suffice, and the simulation takes

less than a second on a PC. However in time-resolved data, like in the case depicted here, the photons needed are many orders of magnitude more. To fully simulate the transmittance of a laser pulse, more than 10^{10} photons should enter the medium resulting in a computing time in the order of one months!.

In our case pulses of 2×10^7 photons each one are launched to the turbid slabs with thicknesses varying from 0.1 to $1.0\,cm$. The refractive index of the medium was chosen to have a value close to that of water i.e. 1.333. Both sides of the slab were modeled to be in contact with the air ($n_{air} = 1$). The quantity measured was the total average intensity transmitted by following the approach described before, for a delta source impinging at $r = (0, 0, 0)$. The anisotropy factor g used in all simulations was $g = 0.8$ for a Henyey-Greenstein [63] phase function, corresponding to realistic values in biological tissues. Other values of g were tested finding no important differences when retrieving the reduced scattering coefficient.

4.3 Phantom preparation

Among the tissue phantoms, resins have the advantage of been solid and therefore easier to handle contrary to the liquid being of Intralipid solutions. The main limitation of resins phantoms resides in the complexity of the preparation procedure, that makes difficult to change the optical properties and geometry of the phantom, as normally required in a research stage. Cubeddu et al. (Ref. [64]) proposed a different approach that compines the ease of an Intralipid solution with the advantages of a solid phantom by adding agar to the liquid solution.

A highly purified agar powder (A-7049, Sigma, USA) is dissolved in distilled water in the appropriate concentration (1%) and heated up to the melting temperature of $95\,^oC$. We bring the mixture to a boil using a microwave oven. The agar solution alone has negligible absorption and very low turbidity. Thus, the desired scattering coefficient of the phantom are reached by adding appropriate amounts of Intralipid (IL) (Pharmacia, Italy), as a scattering medium. With this recipe the absorption coefficient of the phantom can also be adjusted by adding Ink to the solution. In the phantoms used in this work, no Ink or any other additional absorbing chromophore was included in the solution, so that the absorption coefficient remained the same in all samples having a value close to that of water at $800nm$, $\mu_a = 0.02cm^{-1}$. The optimal temperature T_{mix} for adding IL to the agar solution is close to $T_{mix} = 60\,^oC$. The solution is stirred continuously while cooling down to $40\,^oC$, in order to obtain good uniformity. At $40\,^oC$ the solution is poured into the petri-dish and left there for 10 minutes. By following the above-mentioned recipe, three different values of the scattering coefficient were evaluated: $\mu_s' = 5cm^{-1}$, $\mu_s' = 10\,cm^{-1}$ and $\mu_s' = 15\,cm^{-1}$. It is important to note that in the best of cases, the error in determining $\mu_s'$is greater than $\pm1\,cm^{-1}$, i.e. greater than 10% for $\mu_s' = 10\,cm^{-1}$and 20% for $\mu_s' = 5\,cm^{-1}$, which is due to the error given by the used equipment for the preparation of the

samples. For each value of the scattering coefficient, we create phantom slabs with thickness ranging from $0.14cm$ to $1.0cm$. The refractive index of the phantom solution was approximately $n_0 = 1.333$.

Chapter 5

System calibration

In this chapter, the limits of the new theory are explored and a comparison is made with the existing models. In order to characterise thin samples absoption has little contribution and thus the optical characterization can be based on retrieving only the scattering coefficient. The first paragraph of this chapter deals with this assumption. The limits of the new theory are tested with the aid of samples of known optical properties. This method is based on whether the solution of the inverse problem can reconstruct the well defined scattering coefficient of the samples. The theory validation can therefore be performed and the limits of validity can be extracted by pushing thicknesses of the samples to limiting values. Then it is easy to conclude what is the minimum biopsy size in order to be correctly characterized. For the calibration of the theory measurements were performed both in real intralipid phantoms and in numerical ones, derived from Monte Carlo simulations. In the case of Monte Carlo measurements two more theories were tested in limiting geometries and their results were compared with the ones of the modified theory of Chapter 3.

5.1 Absorption contribution

All results presented in this work aim to the estimation of the reduced scattering coefficient μ_s' of thin samples[1]. The reason why the estimation of the absorption characteristics of thin samples (μ_a) is not included can be understood if we take into consideration the different contributions that scattering and absorption have on the measured signal at short distances. Assumed an infinite homogeneous diffusive medium having a reduced scattering coefficient μ_s' and an absorption coefficient μ_a, the detected average intensity at a distance L due to a point source at the origin is [9](see Sec 2.4.2):

[1]If additional parameters such as the anisotropy factor g wish to be retrieved, [65]angular-resolved measurements could also be carried out [66]. Since the main goal of this work was to validate eqs. (3.5.7) and (3.5.8) and obtain the reduced scattering coefficient, such a study was not performed.

$$U(t) = \frac{U_0}{t^{3/2}} \exp\left[-\frac{L^2}{4Dct} - \mu_a ct\right] \tag{5.1.1}$$

where U_0 includes the source strength and other constants. The different contributions can be easily found as:

$$\log\left[U(t)\right] = \log U_0 - \frac{3}{2}\log t - \frac{L^2}{4Dct} - \mu_a ct\,. \tag{5.1.2}$$

From Eq. (5.1.2), it is obvious that the scattering contribution dominates at short times, while the absorption contribution dominates at long times together with an optically-independent contribution of $\log t$. In the infinite homogeneous case considered in Eq. (5.1.1) the time at which the scattering contribution is equivalent to the absorption contribution (t_{abs}) corresponds to:

$$t_{abs} = \langle t \rangle = \frac{L}{2c}\sqrt{\frac{1}{D\mu_a}} \tag{5.1.3}$$

where in the infinite homogeneous case $t_{abs} = \langle t \rangle$. As a practical example, let us consider the case in which $\mu_s' = 10\,cm^{-1}$, $\mu_a = 0.02\,cm^{-1}$, and $n_0 = 1.333$, yielding $D = 0.0333\,cm$. In this case $t_{abs} \sim L\,(cm) \times 10^{-9}\,s$, and for $L = 0.2\,cm$ the intensity of $U(t)$ is 1% of its original value at $t = t_{abs} = 100\,ps$ (obtained from eq. (5.1.2)). This means that at $t = t_{abs} = 100\,ps$ we need to have a noise contribution much lower than 1%, where the total value of $U(t)$ has already decayed to ~ 0.01 of its original value. With our experimental setup we found that the noise contribution in this particular case was in the order of 10%or higher at $t = 100\,ps$. This did not allowed any chance of retrieving the absorption coefficient from experimental measurements.

The above-mentioned relationships do not imply that the estimation of the absorption coefficient is not feasible for thin samples. What is implied in this derivation is that retrieving the absorption coefficient from measurements at a single laser wavelength has some inherent limitations and very high signal to noise ratios are needed. If a scan over a range of wavelengths where $U(t)$ exhibits wavelength dependence is performed, then relative measurements will permit the retrieval of both the reduced scattering and the absorption coefficients .

The reason of not taking under consideration the absorption coefficient can be understood from a biological perspective, too. Since the absorption of tissue is strongly associated with presence of blood, the absorption coefficient of the excised sample cannot be related with its actual in vivo value because of the extensive loss of blood. In order to combine the results the ex vivo characterization with the in vivo properties only the scattering coefficient can provide reliable information. Regarding this issue there are several factors that change the μ_s': the pH, and the water content. The water content is associated to "shrinkage" of the samples. this may induce changes in the volume in the order of less than 5%, which yields changes in the μ_s'within the experimental error (~10%).

5.2 Data Analysis

As mentioned before, the main goal in this study is to retrieve the reduced scattering coefficient μ_s' from Monte Carlo and experimental data. In order to do so, time dependent curves of our theoretical model that express transmitted intensitty were fitted to experimental curves. Any fitting procedure is based on the minimization of a cost function. I used a multidimensional unconstrained nonlinear minimization (Nelder-Mead) approach to find the minimum of the cost function. This cost function was defined in the frequency domain as:

$$X_\omega = \frac{1}{N_\omega}\sqrt{\sum_{i=1}^{N_\omega}\left(\frac{\left|\widetilde{T}_{slab}^{(exp)}\left(\mathbf{K}=0,\omega_i\right)\right| - \left|T_{slab}^{(th)}\left(\mathbf{K}=0,\omega x_i\right)\right|}{\left|\widetilde{T}_{slab}^{(exp)}\left(\mathbf{K},\omega_i\right)\right|}\right)^2} \tag{5.2.1}$$

and in the time domain as:

$$X_t = \frac{1}{N_t}\sqrt{\sum_{i=1}^{N_t}\left(T_{slab}^{(exp)}\left(t_i\right) - T_{slab}^{(th)}\left(t_i\right)\right)^2}\frac{1}{\left\langle T_{slab}^{(exp)}\left(t\right)\right\rangle} \tag{5.2.2}$$

where (th) and (exp) stand for theoretical and experimental, respectively. N_ω and N_t are the total number of experimental measurements in frequency and time domain, respectively. These were found for those frequencies (ω) and time (t) values such that:

$$\omega_i : \forall\omega \leq 2\Delta\omega \tag{5.2.3}$$

and

$$t_i : \forall t \rightarrow T_{slab}^{(exp)}\left(t\right) > \varepsilon_{thresh}\xi \tag{5.2.4}$$

where $\Delta\omega$ is the Full Width at Half Maximum (FWHM) of $\widetilde{T}_{slab}\left(\mathbf{K}=0,\omega\right)$, ξ is the noise present in the measurement and ε_{thresh} is a threshold value that was set at 10.

Two points should be stated concerning eqs. (5.2.1) and (5.2.2). First, Eq. (5.2.1) assigns equivalent weights to all frequency values, the high frequencies therefore contributing to the cost function in the same manner as the low frequencies. Second, Eq. (5.2.2) assigns greater weights to high values of the transmitted intensity in the time-domain, the short time contributions contributing in a greater manner to the total cost function (see Sec. 5.1). Eq. (5.2.2) is normalized to the mean transmitted intensity $\left\langle T_{slab}^{(exp)}\left(t\right)\right\rangle$ in order to have the same dimensionless character as eq. (5.2.1). The cost function that was finally used in the fitting process consisted on a combination of both eqs. (5.2.1) and (5.2.2):

$$X = \frac{1}{2}\left(X_\omega + X_t\right) \tag{5.2.5}$$

The reason for using a combination of two cost functions is that it yielded more robust solutions than eq. (5.2.1) or eq. (5.2.2) alone. Normalized data were used for the fitting procedure, where the reduced scattering coefficient μ_s', and the A factor, as defined in Eqs. (3.4.1), (3.4.2) were used as fitting parameters. To ensure robustness a normalization factor was allowed to change in the vicinity of 1, and the time delay between the experimental and theoretical curve was left as a free parameter. With the above parameters the total number of fitting parameters is four. However, the normalization factor and the time delay do not play a role in the value of $\mu_s'$and simply ensure that the fitting procedure reaches the absolute minimum and not a local minimum.

In all cases studied the initial values were always $\mu_s' = 30\,cm^{-1}$and $A = 0$. This proves the robustness of the fitting process, since no a priori knowledge on the reduced scattering coefficient is needed. As mentioned in Section 5. 1, when including μ_a as a third fitting parameter we found that its value could vary from $0.02\,cm^{-1}$ to $0.1\,cm^{-1}$ introducing changes in the retrieved μ_s' of less than 10%, within the inherent error of the fitting procedure. Having in mind that the reduced scattering coefficient of the phantoms is not known to a more than 10% even if great care is taken when preparing the samples, then the contribution of absorption lies within the minimum experimental error. Moreover, the retrieved values for the phantoms in Section 5.4 lie in the order of 10% within th erange defined by the error bars. This underlines the already mentioned fact that the contribution of absorption in normalized measurements falls under the noise threshold. At this point it should be stated that whenever using other solutions such as the Method of Images [9] to the slab geometry in the case of thin samples, none of the cost functions presented here had an absolute minimum near the expected value. In these cases it was always necessary to use as initial values the expected ones.

Finally, the impulse response H of the experimental system (the lens/Streak Camera/CCD setup in the experimental case, and the time discretization in the Monte Carlo simulation) was included through convolution of the measured impulse response with the analytical expressions eqs. (3.5.7), (3.5.8):

$$\overline{T}_{slab}^{(th)}(t) = H(t - t') * T_{slab}^{(th)}(t') \tag{5.2.6}$$

which has a straightforward implementation in the frequency-domain:

$$\overline{T}_{slab}^{(th)}(\mathbf{K} = 0, \omega) = \widetilde{H}(\omega)\, T_{slab}^{(th)}(\mathbf{K} = 0, \omega) \tag{5.2.7}$$

These expressions where included in eqs. (5.2.1) and (5.2.2). In the Monte Carlo case a Gaussian pulse with FWHM equivalent to the discretization time $\sim 1\,ps$ was used as an impulse response. In the experimental setup, the FWHM of the incident pulse was measured to be in the order of $\sim 8\,ps$. Finally, a reference pulse was recorded before each measurement.

5.3 Monte Carlo Results

The cases considered in this experimental study were $\mu_s' = 5\,cm^{-1}$, $\mu_s' = 10\,cm^{-1}$ and $\mu_s' = 15 cm^{-1}$ for $g = 0.8$. In all cases $\mu_a = 0.02 cm^{-1}$ and the refractive index of the diffusive medium was $n_0 = 1.333$. Since the outer medium (air) has $n_{out} = 1$ (see Fig. 1), the value yielded for the boundary conditions was $C_{in,out} \simeq 5.04$ (see eq. (3.5.1) and Ref. [41]). Each of these cases was studied for the following slab widths: $L = 0.1, 0.2, 0.3, 0.4, 0.5, 0.7$ and $1.0\,cm$ yielding a total of 21 cases.

The analytical expression of the improved theory was put to test against the expression derived from the Method of Images (MI) [9] which, as already mentioned in the theory section, considers a zero intensity at an extrapolated distance[2] $l_{ext} = CD$. This approach is commonly used to describe light propagation in scattering media of thickness greater than $10 l_{tr}$.

We also present an extended version based on the method of images with an exponentially decaying collection of point sources [50] aproaching in this way the correct modeling of the source term used in Chapter 3 for the improvement of the diffusion approximation. This version of the method of images, in the rest of this work will be referred as "exponential source" . In all cases where the method of images (in either form) was employed, 200 source images were used in order to ensure convergence for thin scattering slabs.

The values of scattering coefficient extracted by the above mentioned fitting procedure summarized in Figures (5.3.1), (5.3.2), (5.3.3) where a comparison between the three theories (Improved Diffusion Equation, Method of Images and Exponential Source with the Method of Images) is presented. The figures (5.3.1), (5.3.2), (5.3.3) represent the cases for the reduced scattering coefficient: $5\,cm^{-1}$, $10\,cm^{-1}$ and $15\,cm^{-1}$ respectively.

For the case of $15 cm^{-1}$ the improved theory can extract the value of the scattering coefficient with a discrepency of less than 10% in almost all the thicknesses down to $2 l_{tr}$. The “exponential source” case cannot cannot extract values of teh reduced scattering coefficient close to the expected ones and deviates from errors in the order of 10%for the $L/l_{tr} = 13$ and $L/l_{tr} = 10.5$ to errors of more than 20% for thickness of $L < 8\ l_{tr}$. However it furnishes a better behavior, in general, than the method of image. It has to be mentioned that the reduced scattering coefficient is consistently overestimated within the limits of validity of teh improved theory. This effect is probably due to the limitations of teh diffusion approximation to account properly for the refractive index mismatch at the boundary.

Similar results are found for the $\mu_s' = 10\,cm^{-1}$case. An overestimation of teh correct scattering coefficient can be observed down to $L/l_{tr} = 2$ for the case of teh improved theory. However, it can extract values of the scattering with errors in the order of $\pm 1\,cm^{-1}$for sample thickness down to two transport mean free paths. On the other hand the method of images diverges as we decrease sample thickness, having a limit equal to $10 l_{tr}$. The “exponential source” expression

[2] A study of the implementation of different boundary conditions by using the MI can be found in ref. [67]

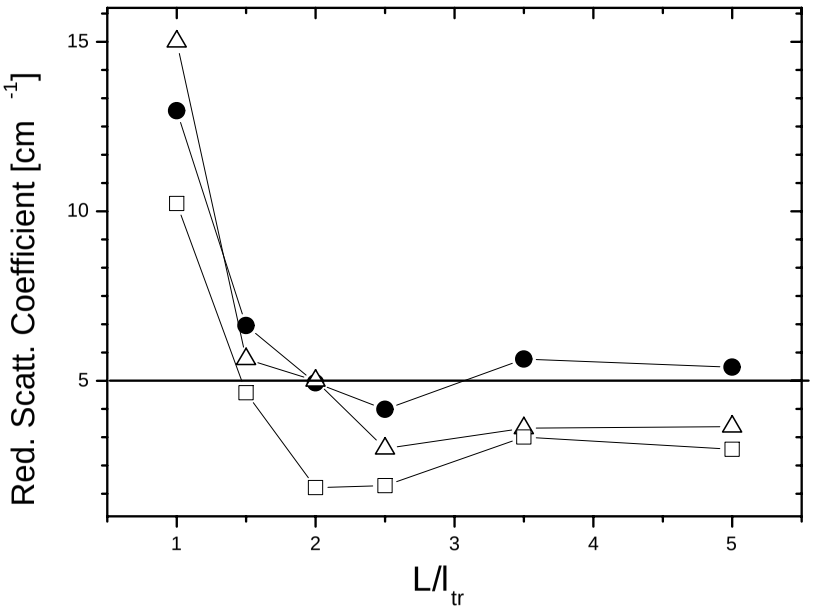

Figure 5.3.1: Retrieved μ_s'values from Monte Carlo simulations by using Improved diffusion theory (bullets), exponentially decaying source applied throught the Method of Images (MI) (triangles) and Method of Images for a point source (squares) versus the normalized slab width $L/l_{tr}$for $\mu_s' = 5\, cm^{-1}$.

(theory) furnishes a slightly better behavior than the MI, hhowever the errors for the scattering coefficient are clearly more than $\pm 2\, cm^{-1}$.

Two transport mean free paths is also the limit for the improved theory regarding the Figure (5.3.1) where the case of $5\, cm^{-1}$is examined. The error again lies within 20%but the other two theories furnish even greater discrepencies. The exponentially source and the MI yielded suprisingly good extracted values for the cases of $L/l_{tr} = 1.5$ and $L/l_{tr} = 2$ respectively. However this is due to the trend that the reconstructed values follow as can be seen in Fig. (5.3.1). In the same way as in the above two cases, the exponential source seems to behave better than the MI indicating that substitution of the delta source by a decaying line source is a step forward towards improving the accuracy of the diffusion theory. There is no other method based on the diffusion theory that can reach the limit of $2l_{tr}$. On the other hand, the limits of validity of teh diffusion approximation in reported experiments are in agreement with the results of Figs. (5.3.1), (5.3.2), (5.3.3) for the method of images case [45].

In reaching the above results, accounting for a frequency dependent diffusion coefficient and an exponentially decaying source with the appropriate boundary conditions plays a crucial role in correctly describing light propagation in limiting geometries. This is better shown in Fig. (5.3.4), which presents the error $\Delta\mu_s'$ in cm^{-1}between the retrieved and the expected value of the scattering coefficient when using the improved theory for the three values μ_s' . There is a

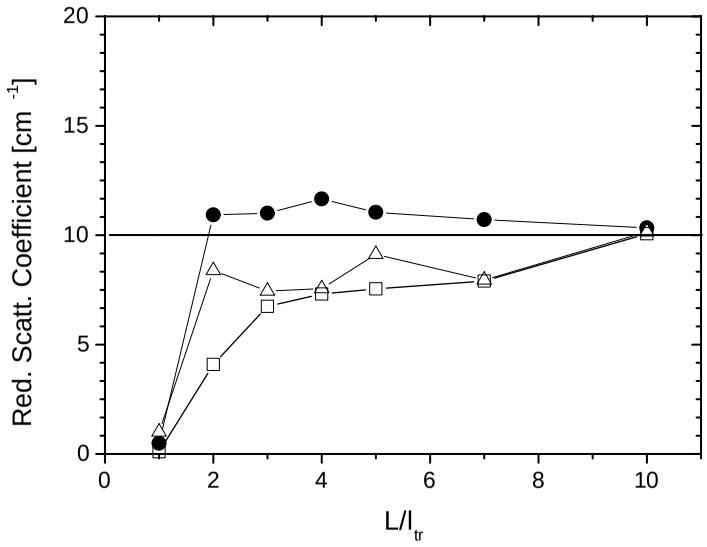

Figure 5.3.2: Retrieved μ_s'values from Monte Carlo simulations by using Improved diffusion theory (bullets), exponentially decaying source applied throught the Method of Images (MI) (triangles) and Method of Images for a point source (squares) versus the normalized slab width $L/l_{tr}$for $\mu_s' = 10\, cm^{-1}$.

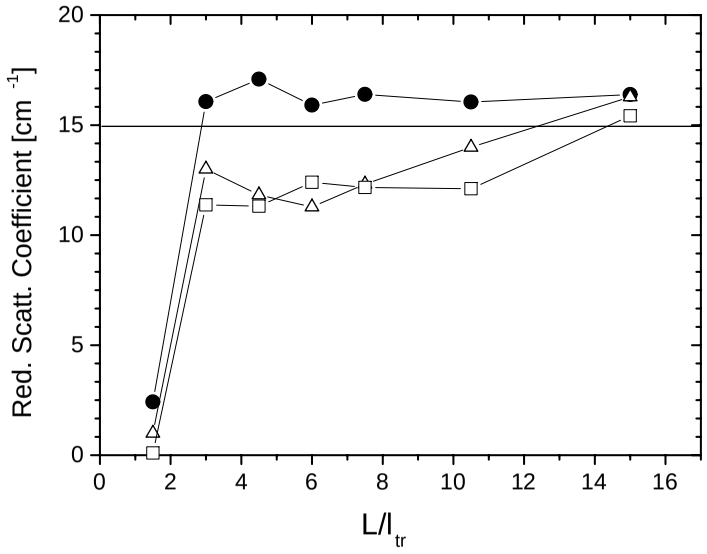

Figure 5.3.3: Retrieved μ_s'values from Monte Carlo simulations by using Improved diffusion theory (bullets), exponentially decaying source applied throught the Method of Images (MI) (triangles) and Method of Images for a point source (squares) versus the normalized slab width $L/l_{tr}$for $\mu_s' = 15\, cm^{-1}$.

sharp threshold value after which the teory yields cinstant fitting values. The improved theory starts to hold for length scales $L \geq 2l_{tr}$ where all errors are within $\Delta\mu_s' \sim \pm 1\, cm^{-1}$. For smaller geometries, propagation is governed by a large ballistic component (was found to be more than 90%) where the contribution of the scattering properties of the medium are very hard to retrieve from single normalized measurements.

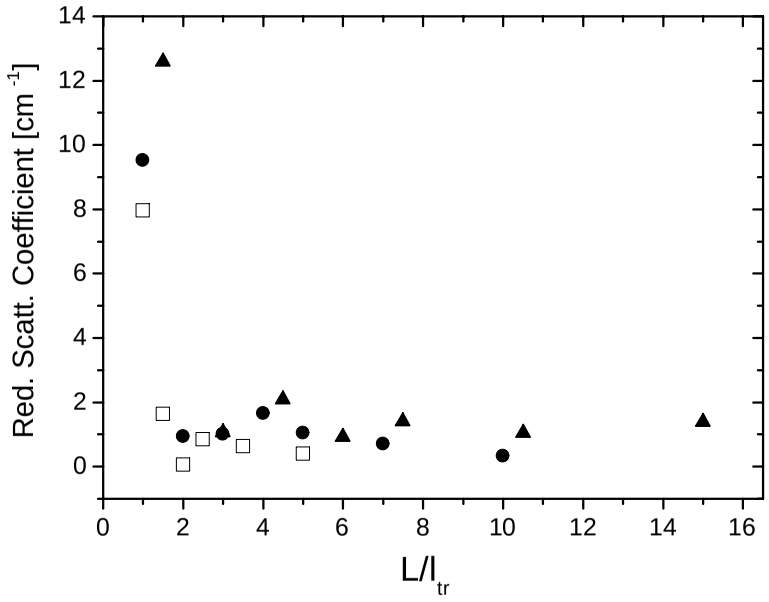

Figure 5.3.4: Deviation of retrieved values from the expected ones for the Figures (5.3.1), (5.3.2) and (5.3.3).

5.4 Phantom results

Measurements were also carried out on phantoms with varying thickness. The Intralipid slabs had a thickness that varied approximately from $0.14\, cm$ to $1.0\, cm$. For each case, three values of the scattering coefficient were generated: $\mu_s' = 5\, cm^{-1}$, $\mu_s' = 10\, cm^{-1}$, and $\mu_s' = 15\, cm^{-1}$. The refractive index of the phantom solution was approximately $n_0 = 1.333$.

Figures (5.4.2) and (5.4.2) presents the retrieved values of μ_s' from experimental data for different slab widths L for the cases $\mu_s' = 10\, cm^{-1}$ and $\mu_s' = 15\, cm^{-1}$ respectively . As shown in this figure, the experimental results reproduce those predicted by Monte Carlo where we observe that the improved theory yields constant error values of $\Delta\mu_s' \approx \pm 1\, cm^{-1}$ for $L \geq 2l_{tr}$. The error values lie within the errors due to the used equipment for the preparation of the phantom samples (Section 4.3). We also applied the method of images and the exponential

source expression in the measurements with the above phantoms. The limit for retrieving the correct reduced scattering coefficient in the case of the phantoms with $\mu_s' = 15\, cm^{-1}$ is approximately 8.5 transport mean free paths for the method of images and ~ 5 transport mean free paths for the case of the "exponential source". For the phantoms with reduced scattering coefficient of $10 cm^{-1}$the limit for the method of images is ~ 10 transport mean free paths while the "exponential source" correctly retrieves the reduced scattering coefficient down to 8 transort mean free paths. Similar experiments took place for samples with $\mu_s' = 5\, cm^{-1}$, but in this case the FWHM of the transmitted intensities was almost equivalent to the FWHM of the incident pulse. Therefore, the temporal resolution of our system was not enough to characterize samples of $L < 4\, mm$ for $\mu_s' = 5\, cm^{-1}$. This can be better understood if we refer to Fig. (5.4.3) where the FWHM versus the normalized sample thickness L/l_{tr} is ploted for $\mu_s' = 5$, 10 and $15\, cm^{-1}$. Since the FWHM of the incident pulse was $\sim 8ps$, it can be seen from Fig. 6 that it is not possible to characterize samples with $\mu_s' = 5cm^{-1}$ for $L \leq 2l_{tr}$.

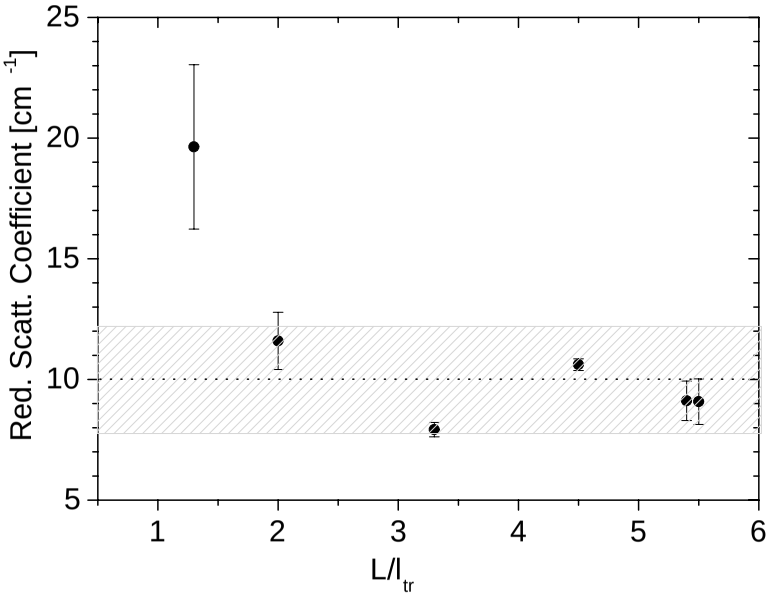

Figure 5.4.1: Experimental retrieved values of μ_s'versus L in mm for $\mu_s' = 10\, cm^{-1}$.

At this point, it should be stated that whenever using other solutions such as the Method of Images [9] to the slab geometry in the case of thin samples, none of the cost functions presented here had an absolute minimum near the expected value. In these cases it was always necessary to use as initial value the expected one.

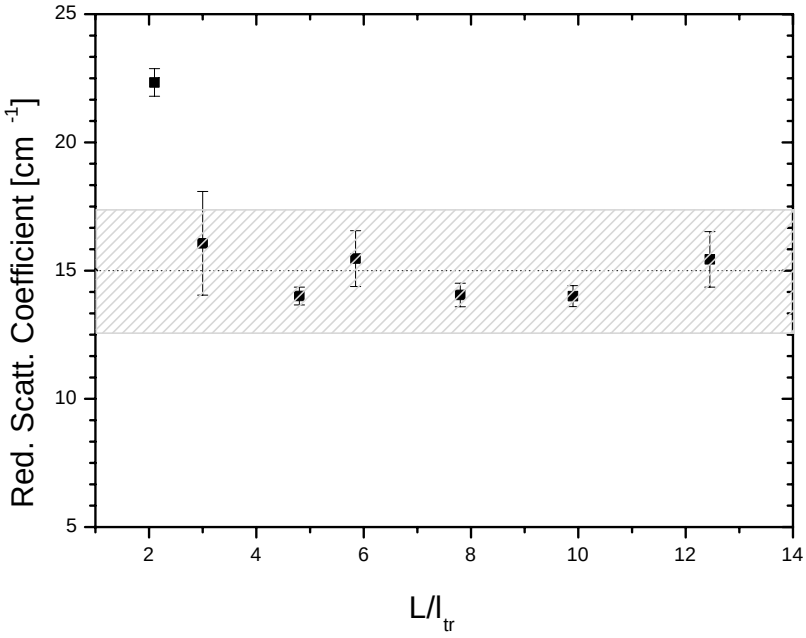

Figure 5.4.2: Experimental retrieved values of μ_s' versus L in mm for $\mu_s' = 15\,cm^{-1}$.

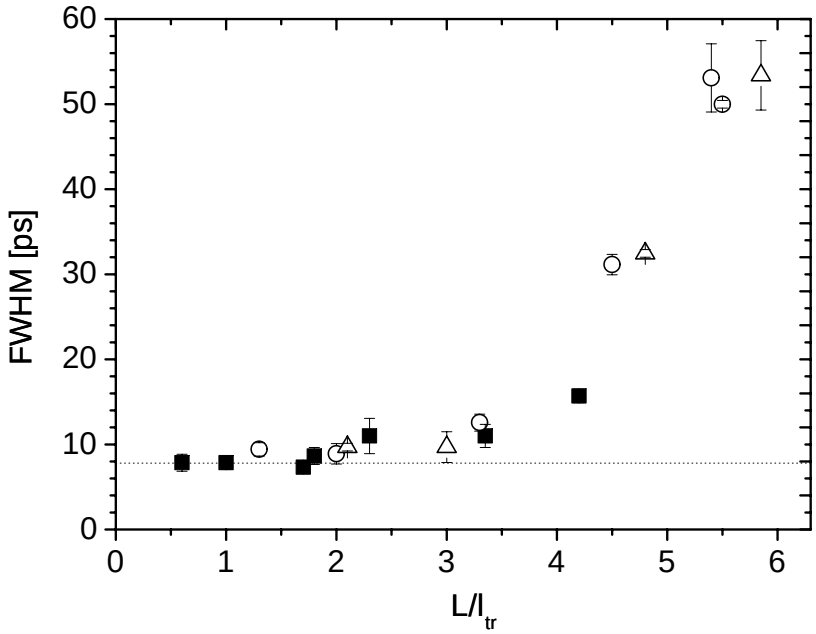

Figure 5.4.3: FWHM retrieved from the experimental configuration versus L/l_{tr} for $\mu_s' = 5$, 10 and $15\,cm^{-1}$. FWHM of the system response H is plotted as a dotted line. In all cases $\mu_a = 0.02\,cm^{-1}$.

5.5 Fitting curves

As mentioned in Section 5.2 the fitting procedure is based on the minimization of the sum of a time dependent X_t and a frequency dependent X_ω cost function. Figure (5.5.1) shows the fitted curves to the experimental data both in time and frequency domain. The experimental data corresponds to a single measurement on a phantom of $L = 2\,mm$ thickness for which the expected values where $\mu_s' = 10\,cm^{-1}$and $\mu_a = 0.02\,cm^{-1}$. As shown in Fig 5.5.1a, the value for the transmitted intensity yields a close fit to the experimental data, even for such a case when the FHWM of the transmitted pulse is in the same order as the incident pulse (shown as a dotted line in Fig. 5.5.1a). More importantly, the retrieved value for μ_s' is within the error predicted by Monte Carlo (Figs. (5.3.1), (5.3.2), (5.3.3)). In this particular case the fitted value for A (energy partition between ballistic and diffusive contribution) was found to be 40%. As mentioned before, the A factor plays an important role when fitting the shape of time curves for thin samples. However, it must be emphasized that the retrieved value of μ_s' did not depend on A, due to the higher contribution of X_ω to the total cost function where A and μ_s' can be considered independent.

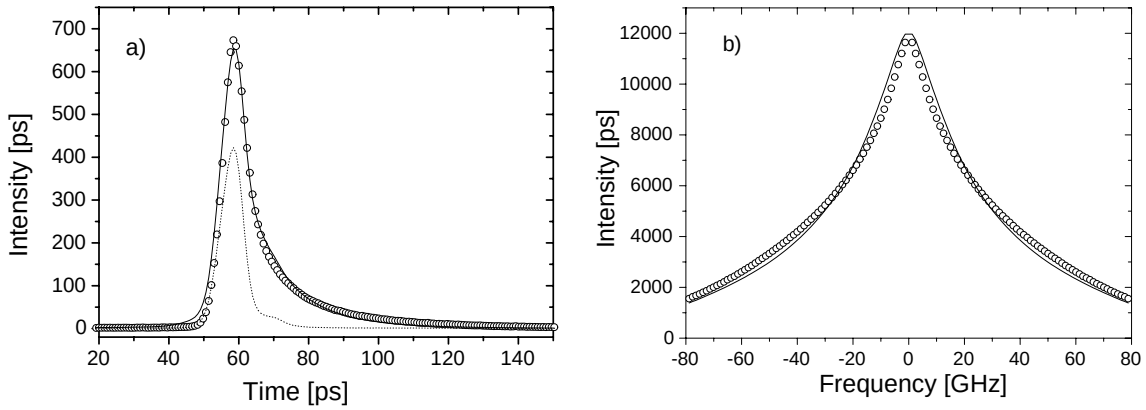

Figure 5.5.1: Fitted values using the improved diffusion approximation (solid lnes) versus experiment (circles) in: (a) time domain; (b) frequency domain. The incident pulse is presented in (a) as a dotted line for comparison. Results presented for $\mu_s' = 10\,cm^{-1}$, $\mu_a = 0.02\,cm^{-1}$and $L = 0.2\,cm$.

Chapter 6

Biopsy characterization

In contrary with the large number of experiments performed in vivo for the determination of the optical properties of breast tissue (Refs. [10, 68, 69, 28, 51, 12]), few experimental data of the in vitro properties have been reported [70, 11, 71, 22, 72]. Moreover even fewer are the measurements upon breast tumors[11]. Chapter 6 is divided in two sections. Section 6.1 is meant to familiarise the reader with some of the aspects of breast physiology and and tissue pathology. Since the main goal of this work was to explore possible correlation of a diseased tissue with its optical properties it would be useful to have an histological insight of the human breast tissue. This will enable better exploration on whether pathological changes may alter the optical properties of tissue. Section 6.2 deals with the biopsy results of the present work. Time resolved measurements were performed to a large number of breast tissue biopsies. The biological samples taken from patients operated at the Epartment of Surgical Oncology of the Univerity Hospital of Heraklion were categorized as tumorous, glandular and fatty according to the histological analysis provided by the Department of Pathology of the University Hospital of Heraklion. The optical properties of glandular and tumorous tissue were derived according to the improved theory previously presented and tested. The negligible scattering of the fat tissue did not permit the extraction of its optical properties. A possible correlation with the age of the patients was also explored.

6.1 Tissue physiology

As mentioned in section 4.2.2 every sample went back to the University Hospital being histologically analyzed. During the measurements on each sample we did have information on the type of tissue we were irradiating. This information was given to us from the pathologist when cutting the samples off the surgical specimen and was based on his experience from macroscopic evaluation of the tissue. However for our analysis we used the results of the final pathologic analysis of our material, which was returned to the Department of Pathology at the end of

our measurements. Discrepancies between the first estimation of the histopathologist and the precise results concerned mainly the normal glandular samples i.e. whether it finally consisted of epithelial or adipose tissue. In Section 6.1.1, the normal breast composition and anatomy are presented, while Section 6.1.2 describes the different kinds of pathologic transformations of the normal tissue associated with this work i.e. ductal carcinoma, DCIS, fibroadenoma. In Section 6.1.3 the origin of light scattering inside the breast is discussed by presenting the most significant light scatterers.

6.1.1 Breast composition

The breast is a mass of glandular, fatty amd fibrous tissues positioned over the pectoral muscles of the chest wall and attached to the skin by fibrous strands called Cooper's ligaments. A layer of fatty tissue surrounds the breast glands and extends throughout the breast. The fatty tissue gives the breast a soft consistency. The glandular tissue of the breast houses the lobules (milk producing glands at the ends of the lobes) and the ducts (milk passages). Towards the nipple, each duct widens to form a sac (ampulla). During lactation, the bulbs on the ends of the lobules produce milk. Once milk is produced, it is transferred through the ducts to the nipples [73]. The breast anatomy is shown in Fig. 6.1.1.

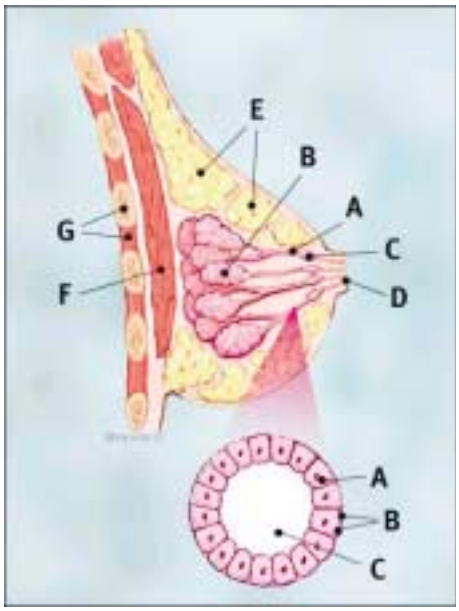

Figure 6.1.1: Schematic representation of the female breast structure: *A*) *ducts*, *B*) *lobules*, *C*) *dilated section of duct to hold milk*, *D*) *nipple*, *F*) *pectoralis major muscle*. Enlargement: *A*) *normal duct cells*, *B*) *basement membrane*, *C*) *center of duct*.

The female breast, being dependent on a variety of hormones for its normal activity, exhibits considerable structural and functional variation through life. Apart from the overt changes occuring at puberty, pregnancy, lactation and menopause, more subtle changes also occur within

the normal cycle; as a result of hormonal variations preparing the body for the possibility of a pregnancy.

6.1.2 Disorders of the breast

Forty percent of patients attending a breast clinic have a benign breast lump. The breast surgeon has two important tasks: to decide if the lump is truly abnormal or falls within the spectrum of normality and if the lump is abnormal to determine its nature (benign or malignant).

Most common conditions presenting as lumps are cysts, fibroadenomas (13% of all palpable lumps, 60% in women less than 25 years of age), fat necrosis (in obese women with large breasts or following trauma), sclerosing adenosis are now considered to represent aberrartions of normal development and involution (ANDI).

Benign breast tumors are epithelial (intraductal papilloma, adenoma) fibroepithelial (benign phyllodes tumor and mammary hamartoma), mesenchymal (lipoma, granular cell tumor, myofibroblastoma, hemangioma, leiomyoma and schwannoma) and tumours of the nipple (adenoma).

Ductal Carcinoma in situ (DCIS) and Invasive Carcinoma

The most frquent type of breast cancer (85% of all breast cancers) is the ductal carcinoma arising from the epithelium of the breast ducts, but which have not yet invaded through the basement membrane, ae known as carcinoma in situ (DCIS).

The are various types of non invasive ductal carcinoma (comedo, cribriform, micropapillary, solid) and DCIS often occurs as a mixture of the different types. Certain types of DCIS are associated with characteristic microcalcifications fiving confined by the basement membrane can not give metastases since the vessels are situated below membrane.

Invasive ductal carcinomas surrounded by an extensive intraductal component (EIC) are more likely to be multifocal and are often more difficult to remove. Great care needs to be taken to ensure that both the cancer and the extensive in situ component are excised.

Many more patients with DCIS are now being diagnosed after the implementation of breast screening. The increase has been across all age groups with a 12% annual increase in the 30-39 year age group and a 15% annual increase in women over the age of 50. Whether the increase and detection of these early lesions will reduce the subsequent encidence of invasive cancer is not yet evident, although it is likely to do so.

Fibroadenoma

It is considered to be an aberration of normal breast development most commonly presenting between 15 and 25 years of age but seen up to 35 years of age. Its incidence decreases on menopause when they involute. Fibroadenomas arise from a single lobule and are affected by

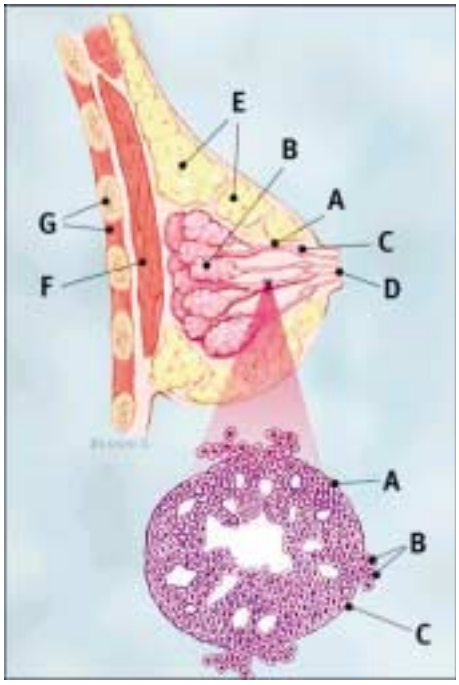

Figure 6.1.2: Infiltrating ductal carcinoma: *A) ducts, B) lobules, C) dilated section of duct to hold milk, D) nipple, F) pectoralis major muscle.* Enlargement: *A) normal duct cells, B) ductal cancer cells breaking through the basement membrane, C) basement membrane, D) center of duct*

hormonal changes thus do not represent a true tumor. They are of unknown etiology which might include hypersensitivity to oestrogen within a lobule. They are usually less than 2 cm and rarely up to 3 cm. Those which grow more than 5 or 10 cm are considered as juvenile breast disease. On clinical examination they are smooth, slightly lobulated and characteristically mobile (except if close to nipple). Their histology consists of intralobular fibrous stroma enclosing glandular spaces with epithelial lining.

For their diagnosis up to 25 years clinical impression suffices. While in patients older than 25 years a triple assessment confirmation is needed. Conservative approach may result in a small number of missed cancers, so removal is generally recimmended after the age of 25.

6.1.3 Significant light scatterers in the human breast

As in all biological tissues, all cellular and extracellular components of the breast tissue contribute to light scattering; however, the relative magnitude of each component has not been measured.

The membrane-bound subcellular organelles such as the nuclei ($6-8\,\mu m$) in noncancerous breast epithelial cells), mitochondria (less than $1\,\mu m$), secretory vacuoles ($1-10\,\mu m$) and other similarrly sized intracytoplasmic granules can influence light scattering because of refractive index differences at membrane interfaces. As has been suggested, differences in the refractive

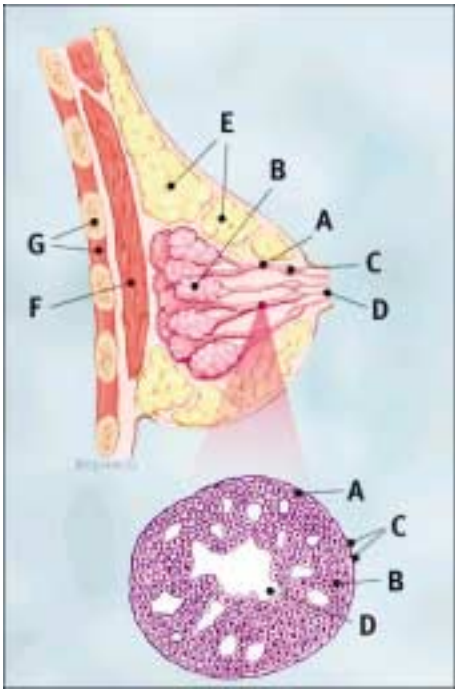

Figure 6.1.3: Ductal Carcinoma In Situ: *A) ducts, B) lobules, C) dilated section of duct to hold milk, D) nipple, F) pectoralis major muscle.* Enlargement: *A) normal duct cells, B) ductal cancer cells, C) basement membrane, D) center of duct.*

indices may be due also to differences in water content of the different organelles. However, another possible mechanism to explore is that refractive differences exist between water-rich cytoplasm and the relatively hydrophobic lipoprotein layers of the cellular and organelles membranes [74].

Collagen is the predominant scatterer of the extracellular stromal matrix of the breast. The 3-dimensionally arranged interfaces between the glandular and adipose tissues and bands of fibrous collagenous tissue may form optically anisotropic boundaries that could influence light transport into the depths of the breast. However, collagens (and elastins) have complex molecular interactions with water, salts and proteoglycans of the extracellular matrix in vivo and these interactions change with age and hormonal status. These interrelationships produce complex water-based chemical neighborhoods that probably influence light scattering by collagen in vivo [74].

6.2 Biopsy results

In Chapter 3 the theoretical assumptions that correctly predict light propagation in small geometries were put forward improving thus the standard diffusion equation. The limits of our theory were explored in Chapter 5 where experimental measurements were performed on both Monte Carlo simulations and phantom samples. It was found that the improved theory can

correctly predict not only the reduced scattering coefficient but also the temporal profile for samples with thickness in the order 2 transport mean free paths. However as will be shown in the following sections a relative large number of samples had thickness of less than 2 transport mean free paths. The reason is that histopathologists could not provide relatively big samples for the cases where the tumor was quite small. In these cases the removal of even a small portion would have compromise a precise diagnosis. Moreover theory development was performed together with biopsy measurements and therefore, precise limits of its validity could not be extracted. Subsection 6.2.1 offers a statistical view of the sample thickness and sample physiology. The task of retrieving those the samples that satissfy the thickness creterium is also discussed. In subsection 6.2.2 the tumor samples were characterized and analyzed and the retrieved values were compared with known values from the literature. Also a possible correlation of tissue pathology and demographics is investigated. A similar analysis is also performed in Section 6.2.3 for the case of glandular tissue. It should be mentioned that all measurements were performed at room temperature ($22\,^oC$).

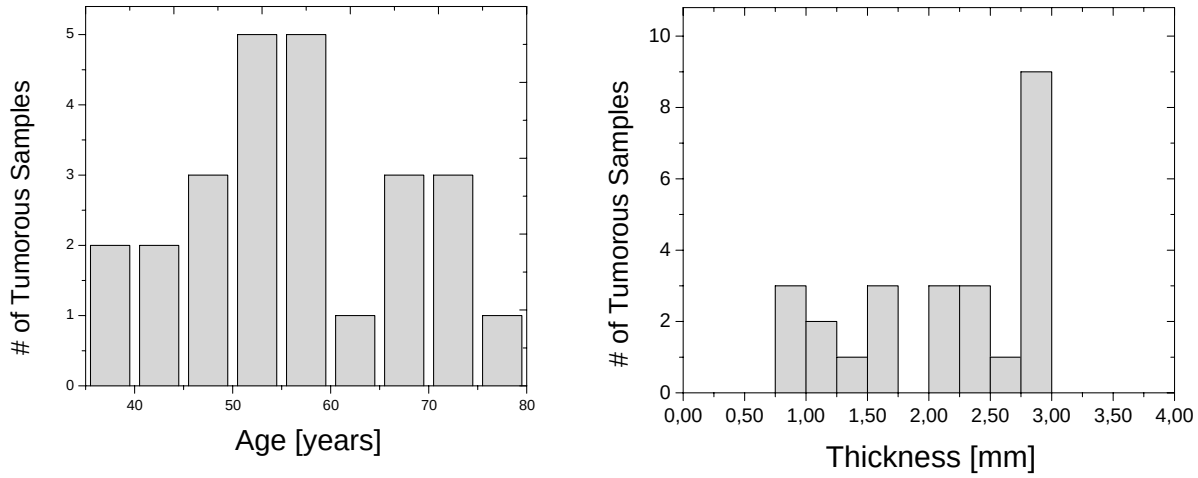

Figure 6.2.1: Sample thickness and age distribution of the patients whose samples were irradiated for the case of tumor tissue. The total number of tumor samples is 25.

6.2.1 Sample characteristics

As mentioned in Chapter 4, samples from a total of 27 patients have been measured. The ages of the patients varied from 35 to 80 years old and the samples obtained can be categorized as glandular, tumorous and fatty. Not in all cases 3 samples were obtained from each patient,

namely a tumorous, a glandular and a fatty. This is the reason why the total number of glandular samples is different from the total number of tumorous ones. The same reason explains differences in the age distributions between the glandular and the tumorous case. The age and thickness distributions in the case of tumorous samples is shown in Fig. (6.2.1)

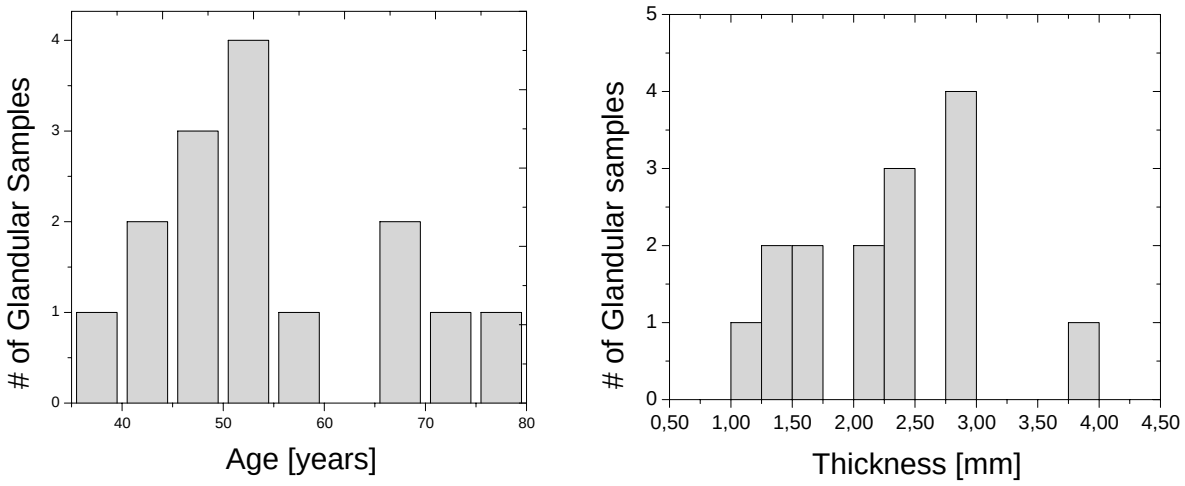

Figure 6.2.2: Sample thickness and age distribution of the patients whose samples were irradiated for the case of glandular tissue. The total number of samples is 21.

For the case of glandular tissue 21 samples were measured and the distributions on age and thickness are presented in Fig (6.2.2). As mentioned before all tissue samples were first measured and characterized and then some of them were discarded according to their thickness and their scattering coefficient (thickness criterion, see Chapter 5). Since the limit of the theory is two transport mean free paths, this means that the thickness limit is $1.33\,mm$ for $\mu_s' = 15\,cm^{-1}$and $2\,mm$ for $\mu_s' = 10\,cm^{-1}$. More generally $L/l_{tr} \geq 2$ or equivelantly (Fig. (2.1.9)) $L\mu_s' \geq 2$. For each type of tissue plots of the reduced scattering coefficient versus the thickness were performed together with the function $\mu_s' = 2/l$. This is shown, for the case of fatty tissue, in Fig. (6.2.3) . The shaded area represents the region where the theory does not hold. As it can be seen, a small number of samples satissfy the scattering criterium. It should be mentioned that in fatty samples laser pulses suffer negligible scattering as they propagate inside them. In general, collagen-rich glandular tissue scatters light with a higher scatter power than adipose tissue. Thus, smaller scatter powers are expected in fatty tissue. This combined with the small thickness leads to transmitted temporal profiles with FWHM compared to the ones of the incident pulses (Fig. (6.2.3)). Values of the reduced scattering coefficient from fatty tissues were not analyzed here because only quite small number samples had enough thickness to yield

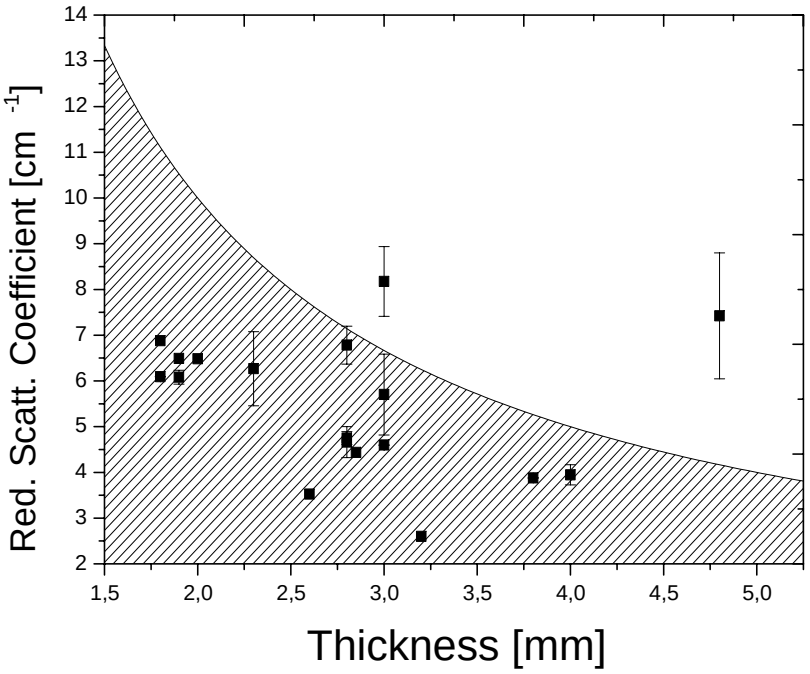

Figure 6.2.3: Correlation of the reduced scattering coefficient with thickness, for the case of fat samples.

statistical valuable results. However, it should be also mentioned that even with this small number of samples the results obtained are in agreement with results reported in the literature (Refs. [11, 22]).

6.2.2 Glandular tissue

Similar to the case of fat tissue, it was first checked which samples are within the limits of the improved theory. The correlation between thickness and the fitted reduced scattering coefficient for the glandular tissue samples is shown in Fig. (6.2.4). The error bars represent the results of repeated measurements. It can be seen that a lot of samples were discarded from the analysis due to the above mentioned criterion.

The retrieved reduced scattering coefficient values for glandular tissue are presented in Fig. (6.2.8), as a histogram. The mean value obtained was $\langle \mu_s' \rangle = 9.7 cm^{-1}$and the standard deviation was found to be $\Delta \mu_s' = 2.2 cm^{-1}$. The above value of the reduced scattering coefficient is clearly bigger than that of fat tissue, demonstrating that glandular tissue is a stronger scatterer for the light.

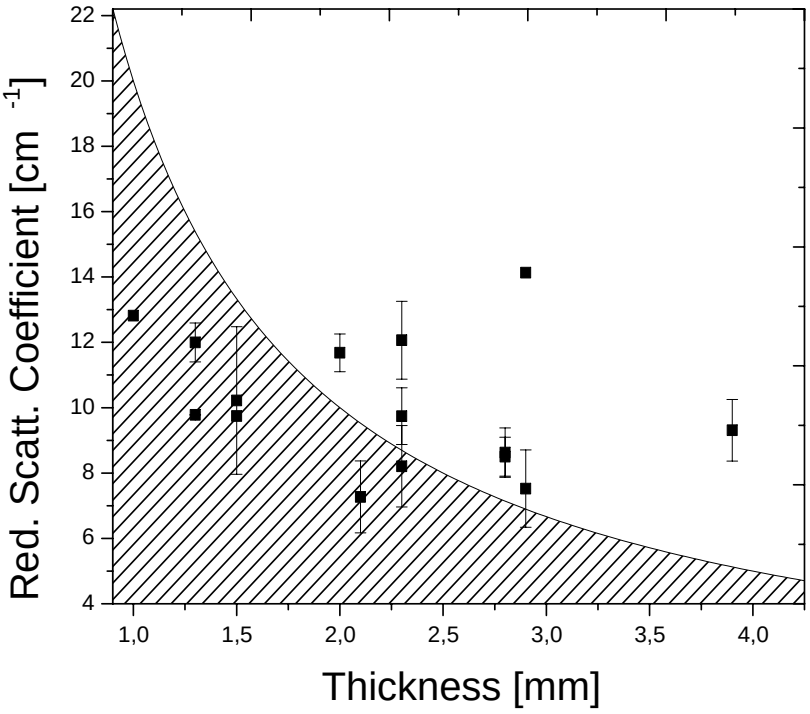

Figure 6.2.4: Correlation of the reduced scattering coefficient with the thickness for the case of the glandular tissue.

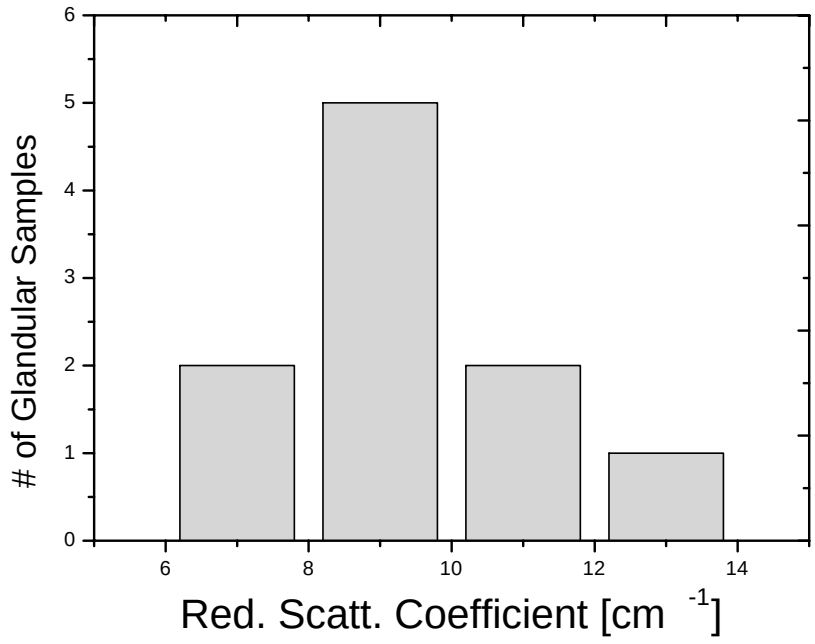

Figure 6.2.5: Distribution of the reduced scattering coefficient for glandular tissue excised from female breast.

Table 6.1 lists literature values of the reduced scattering coefficient for the case of glandular tissue measured in vitro. The results obtained in present work are also shown in the Table (6.1) and are in agreement with other investigators. Moreover in vivo measurements of the bulk properties of female breast tissue have shown similar results (Refs. [10, 68, 69, 28, 51, 12]). From the references presented in the table, only in Zacharakis et al. and Troy et al. studies

Reference	Wavelength (nm)	Temperature(^oC)	μ_s' (cm^{-1})
Peters et al.[11]	900	22	9.9 ± 2.0
Zacharakis et al.[22]	800	22	$\sim 8.8 \pm 0.9$
Gayen and Alfano[71]	800	22	~ 10
Bevilacqua et al.[72]	670	22	$\sim 7.8 \pm 0.8$
Troy et al.[70]	836	37	8.1 ± 2.2
This work	830	22	9.7 ± 2.2

Table 6.1: Literature values of the reduced scattering coefficient in the case of glandular tissue.

concerned a large number of samples so that statistically acceptable results can be derived. In addition, differences in methods influence the results as well. It should be emphasized that a comparison of optical properties measured by different investigators is in general difficult. The breast tissue is a vague concept, given the frequency and magnitude of changes that occur over a variety of time scales. The physiology of healthy breast tissue is influenced by multiple factors

such as menstrual cycle, menopause, exogenous hormones, lactation and pregnancy.

Since the breast, as a subject of tissue optics studies, is so complex it is desirable to measure the properties including the variation with time. Thus far a few investigators have probed such changes with respect to hormone levels during the menstrual cycle [75], menopause [68, 76]and age[12, 76, 68]. All the above measurements were performed in vivo. Fig.(6.2.6)depicts the distribution of μ_s'versus age. The figure shows that there is weak correlation. Prememopausal subjects (i.e. age$<$ 50) display a variety of values. Inter-subject variations include, but are not limited to, menstrual cycle differences and gynecological age. The reduced scattering coefficient of glandular tissue seems to vary in a greater range in premenopausal samples. After age 50 (predominantly postmenopausal) there is a general localization of the reduced scattering variations. The late result can be correlated with the atrophy of well-vascularized lobular tissue and the increase of the fat-to-collagen ratio after menopause[77].

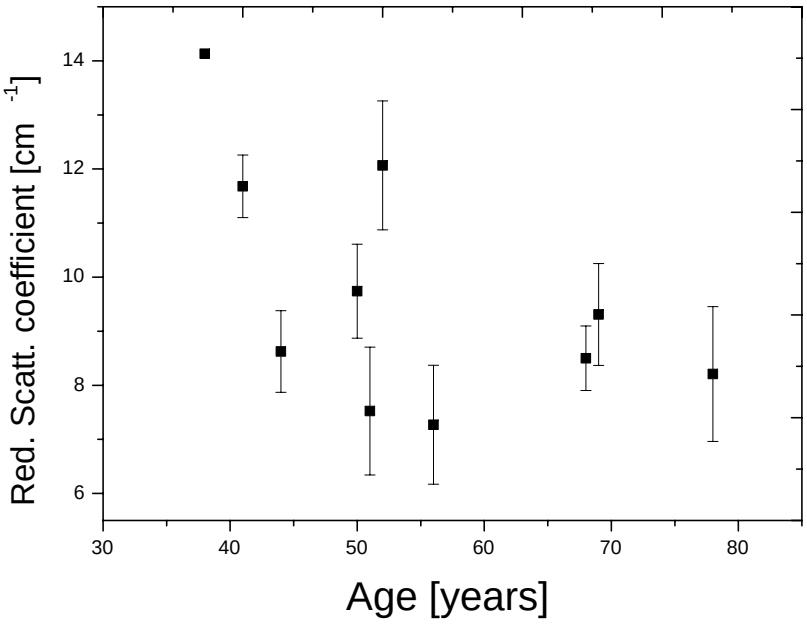

Figure 6.2.6: Correlation of reduced scattering coefficient with age for the case of glandular tissue

6.2.3 Tumor tissue

A similar study to that carried out on the previous section was also performed for the tumorous tissue. Measurements were performed on a total of 27 samples with thickness shown in Fig. (6.2.1). In Fig. (6.2.7) the correlation of the retrieved reduced scattering coefficients with the thickness of the samples is presented. The shaded area represents the region where the theory

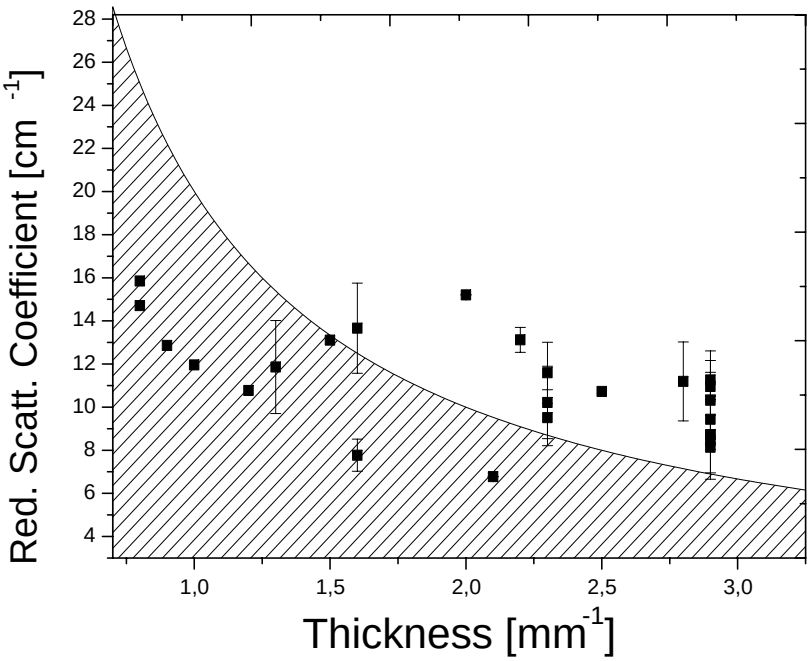

Figure 6.2.7: Correlation of the reduced scattering coefficient with the thickness, for the case of tumor.

deviates. All samples under the shaded region were therefore discarded from further analysis. The samples survived can be classified as infiltrating ductal carcinoma ($n = 15$), fibradenoma ($n = 1$)and ductal carcinoma in situ (DCIS)($n = 1$).The retrieved reduced scattering coefficient values for tumor tissue are presented in Fig. (6.2.8), as a histogram. The mean value obtained was $\langle \mu_s' \rangle = 10.8\, cm^{-1}$and the standard deviation from the histogram was found to be $\Delta\mu_s' = 2.0\, cm^{-1}$. Comparing these results with the ones of glandular tissue, there is no significant statistical difference between the scattering coefficients of tumor and glandular tissue. However, trends do exist since tumors have highest scattering properties. In literature scattering values for breast lesions have been measured in vitro to be both lower and higher than normal tissue as can be seen in table (6.2). The nature of these differences is not clear, however it can be related with differencies in techniques and conditions of each study.

Reference	Wavelength (nm)	Temperature(^oC)	μ_s' (cm^{-1})
Peters et al.[11]	900	22	8.9 ± 2.6
Gayen and Alfano[71]	800	22	~ 10
Troy et al.[70]	836	37	10.5 ± 2.7
This work	830	22	10.8 ± 2.0

Table 6.2: Literature values of the reduced scattering coefficient in the case of tumorous tissue

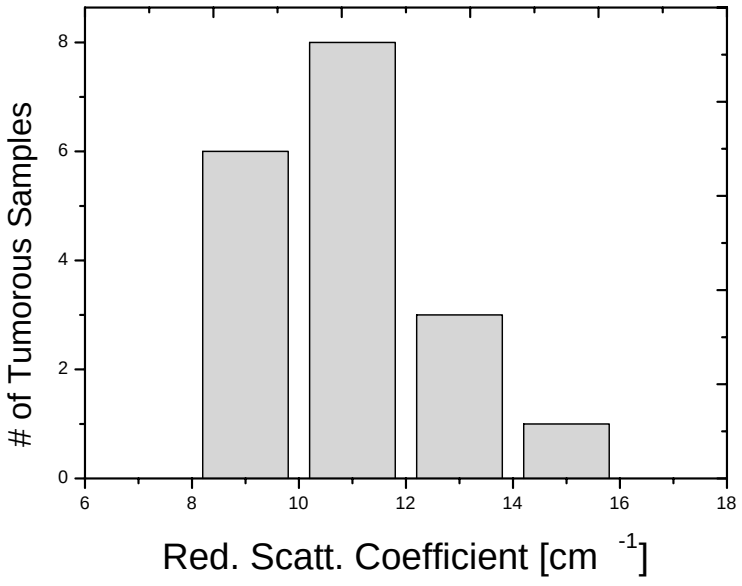

Figure 6.2.8: Distribution of values of the reduced scattering coefficient for tumor tissue excised from female breast.

The correlation of the reduced scattering coefficient with age for the case of tumorous tissue is presented below where results show no correlation between both. Finally, it is not clear from

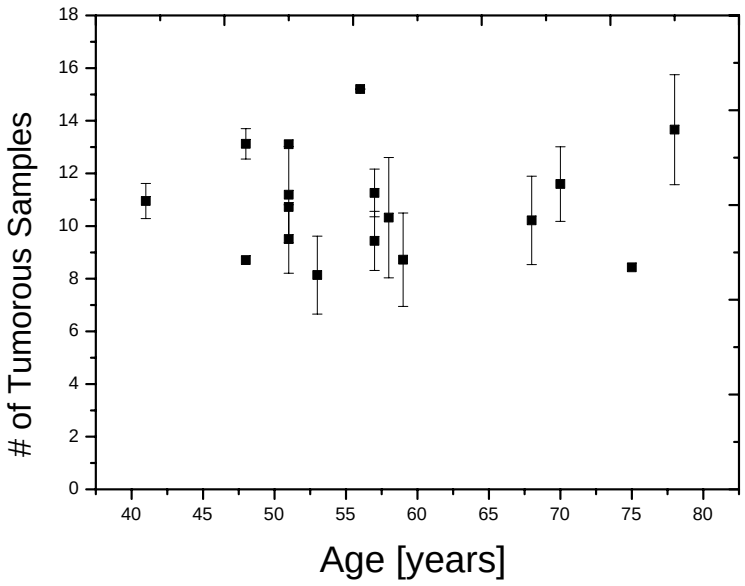

Figure 6.2.9: The correlation of the reduced scatterning coefficient with the age for the case of tumorous tissue

the above studies how the optical properties of various types of biological tissue differ from each other in vivo.

Chapter 7

Conclusions

A novel analytical expression for light propagation in scattering media based on an improvement of the diffusion approximation has been presented. This approach takes into account a frequency-dependent diffusion coefficient and dynamic boundary conditions that predict that photons do not diffuse instantly. By using this model with an exponentially decaying source, an analytical solution for a slab of arbitrary width by means of the reflection and transmittance coefficients for diffusive waves taking into account the boundary conditions rigorously was derived.

The most common expression for the treatment of the source part of the diffusion equation is a delta function. This delta function implies isotropic emission of light even in configurations where the sample is illuminated by a clearly anisotropic source such as a laser pulse incident on a diffusive slab. It has been shown in many cases that the point source approximation yields accurate results when measurements take place far away from sources and boundaries [9]. However, as shown in this work in the range of sample thickness comparable to the mean free path, the need to account for the correct source term is critical for obtaining accurate results. The actual source created by a laser pulse incident onto a scattering medium is the solution to the Radiative Transfer Equation in the absence of multiple scattering yielding a source which is not a delta function but rather a line whose strength decreases exponentially with depth.

The diffusion equation can be further improved by introducing a dynamic diffusion coefficient. When dealing with short times, it is important to consider that photons do not diffuse instantly, as stated by the standard diffusion equation. Here, a frequency dependent diffusion coefficient has been proposed and validated within the experimental accuracy showing that this dependence must be included for accurate results to be obtained.

Moreover, when dealing with small samples the need to accurately account for the presence of boundaries implies that correct expressions for the reflection and transmittance coefficients are of major importance. With the aid of the reflection and transmission coefficients for diffusive/non-diffusive interfaces [58] the boundary conditions are correctly treated enabling

	$\mu_s'(cm^{-1})$
Tumor Tissue	10.8 ± 2.0
Glandular Tissue	9.7 ± 2.2

Figure 7.0.1: Average reduced scattering coefficient and standard deviation of tumorous and glandular tissue, measured in vitro.

the straightforwardly solution for the slab geometry. All the above assumptions for the source, diffusion coefficient and boundary conditions allow the derivation of an analytical expression for the temporal and spatially dependent transmittance and reflection from a slab. With this expression light propagation is accurately described even at short length and time scales, while retaining the computational efficiency and simplicity of the diffusion approximation.

This theory has been tested against Monte Carlo simulations showing that the reduced scattering coefficient of thin samples can be obtained with good accuracy for widths down to $2l_{tr}$. In all widths down to $2l_{tr}$the error is in the order $1\,cm^{-1}$independent on the value of μ_s', which leads to have a systematic error in μ_s'. Two other theories have been compared against the improved theory, namely the Method of Images and a version of the Method of Images with an exponentially decaying source term, but showed discrepancies in small length scales. Since the validity and the accuracy of the improved theory was assessed with the Monte Carlo method and found to be the one that had the better performance, experiments were performed in real phantoms in order to examine the limits of the best theory under real experimental conditions. The improved theory reproduced the results predicted by the Monte Carlo simulations except in the case of $\mu_s' = 5\,cm^{-1}$where the FWHM of the transmitted intensities was almost equivalent to the FWHM oh the insident pulse.

Once the theory has been validated and its limits of validity found, small scattering samples like biopsies can be treated properly. In the present work biopsies from a great range of thickness and ages have been measured ex-vivo with time resolved spectroscopy. The types of biopsy samples were glandular, tumorous and fatty. Within the theory described here, characterization of small biopsy samples yields accurate results, as long as the samples have $L/l_{tr} > 2$. Samples not holding this criterion, from every type of tissue, were discarded from further analysis. From the above mentioned types of tissue fat scatter less the light at $830\,nm$.

Regarding the glandular tissue the correlation with the age showed that the reduced scattering coefficient varies with age between pre- and post- menopausal samples. The reduced scattering coefficient for the case of glandular tissue obtained values are presented in Table (7.0.1) together with the values for the case of tumor. The results in Table (7.0.1)show a partly overlap when characterizing in-vitro breast components. Moreover since both the in vivo healthy breast properties at $\sim 830\,nm$ have similar values [10, 68, 69, 28, 51, 12], this means that the reduced scattering will not yield enough contrast in order to discern tumor tissue from the back-

ground when performing diffuse optical tomography. However, in order to extract an absolute conclusion, characterization of the reduced scattering should be performed at greater range of wavelengths. Moreover the absorption coefficient of the surrounding tissue might play a critical role when performing tomographic or spectroscopy studies in cases of neo-vascularization that is when the tumor itself stimulates the growth of new vessels. The data also show an increased scattering coefficient of tumor tissue relative to fatty and glandular tissues. Finally the tumor tissue showed no correlation with the age of patients.

Bibliography

[1] S. R. Arridge, "Optical tomography in medical imaging," *Topical review in Inverse Problems* **15**, pp. R41–R93 (1999).

[2] Ntziachristos, V. and Yodh A. G. and Chance, B., "Concurrent MRI and diffuse optical tomography of breast after indocyanine green enhancement," *Proc. Natl. Acad. Sci. U.S.A.* **97**, pp. 2767–2772 (2000).

[3] V. Ntziachristos and A. G. Yodh and M. Schnall and B. Chance, "MRI-Guided diffuse optical spectroscopy of malignant and benign breast lesions," *Neoplasia* **4**, pp. 347–354 (2002).

[4] Pogue, B. and Poplack, S. and McBride, T. and Wells, W. and Osterman, K. and Osterberg, U., "Hemoglobin imaging of breast tumors with near-infrared tomography," *Radiology* **214**, p. G05H (2000).

[5] Pogue, B. W. and Poplack, S. P. and McBride, T.O. and Wells, W. A. and Osterman, U. L. and Osterberg, U. L. and Paulsen, K. D., "Quantitative hemoglobin tomography with diffuse near-infrared spectroscopy: pilot results in the breast," *Radiology* **218**, pp. 261–266 (2001).

[6] S. Chandrasekhar, *Radiative transfer*. New York: Oxford University Press (1960).

[7] A. Ishimaru, *Wave Propagation and Scattering in Random Media*, vol. 1. New York: Academic (1978).

[8] A. Yodh and B. Chance, "Spectroscopy and imaging with diffusing light," *Phys. Today* **48**, pp. 38–40, March (1995).

[9] M. S. Patterson and B. Chance and B. C. Wilson, "Time resolved reflectance and transmittance for the non-invasive measurement of tissue optical properties," *Appl. Opt.* **28**, pp. 2331–2336 (1989).

[10] Tromberg, B. J. and Shah, N. and Lanning, R. and Cerussi, A. and Espinoza, J. and Phain, T. and Svaasand, L. and Butler, J, "Non-invasive in vivo characterization of breast tumors using photon migration spectroscopy," *Neoplasia* **2**, pp. 26–40 (2000).

[11] Peters, V. G. and Wyman, D. R. and Patterson, M. S. and Frank, G. L., "Optical properties of normal and diseased human breast tissues in the visible and near infrared," **35**, pp. 1317–1334 (1990).

[12] Cerussi, A. E. and Jakubowski, D. and Shah, N. and Bevilacqua, F. and Lanning, R. and Berger, A. J. and Hsiang, D. and Butler, J and Holcombre, R. F. and Tromberg, B. J., "Spectroscopy enhances the information content of optical mammography," *J. Biomd. Opt.* **7**, pp. 60–71 (2002).

[13] L. H. Wang and S. L. Jacques and L. Q. Zheng, "Mcml-monte carlo modeling of photon transport in multi-layered tissues," *Comp. Meth. and Prog. in Biomed.* **47**, pp. 131–146 (1995).

[14] L. H. Wang and S. L. Jacques and L. Q. Zheng, "Conv - convolution for responses to a finite diameter photon beam incident on multi-layered tissues," *Comp. Meth. and Prog. in Biomed.* **54**, pp. 141–140 (1997).

[15] Alexandrakis, G. and Farrell, T. J. and Patterson, M. S., "Monte carlo diffusion hybrid model for photon migration in a two-layer turbid medium in the frequency domain," *Appl. Opt.* **39**, pp. 2235–2244 (2000).

[16] Swartling, J. and Pifferi, A. and Enejder, A. M. K. and Andersson-Engels, S., "Accelerated Monte Carlo models to simulate fluorescence spectra from layered tissues," *J. Opt. Soc. Am. A* **20**, p. 714 (2003).

[17] Elaloufi, R. and Carminati, R. and Greffet, J. J., "Time-dependent transport through scattering media: from radiative transfer to diffusion," *J. Opt. A: Pure Appl. Opt.* **4**, pp. S103–S108 (2002).

[18] Xu, M. and Cai, W. and Lax, M. and Alfano, R. R., "Photon migration in turbid media using a cumulant approximation to radiative transfer," *Phys. Rev. E* **65** (2002).

[19] van der Mark, M. and van Albada, M. P. and Lagendijk, A., "Light scattering in strongly scattering media: multiple scattering and weak localization," *Phys. Rev. B* **37**, pp. 3575–3592 (1988).

[20] Nieuwenhuizen, T. M. and Luck, J. M., "Skin layer of diffusive media," *Phys. Rev. E* **48**, pp. 569–588 (1993).

[21] M. C. W. van Rossum and Nieuwenhuizen, Th. M., "Multiple scattering of classical waves: microscopy, mesoscopy, and diffusion," *Rev. of Mod. Phys.* **71**, pp. 313–371 (1999).

[22] Zacharakis, G. and Zolindaki, A. and Sakkalis, V. and Filippidis, G. and Papazoglou, T. G. and Tsiftsis, D. D. and Koumentakis, E., "In vivo optical characterization and discrimination of female breast tissue during near infrared femtosecond laser pulses propagation," *J. of Biomed. Opt.* **6**, pp. 446–449 (2001).

[23] R. Aronson, "Photon diffusion coefficient in an absorbing medium," *J. Opt. Soc. Am. A* **16**, pp. 1066–1071 (1999).

[24] Cai, W. and Xu, M. and Lax, M. and Alfano, R. R., "Diffusion coefficient depends on time, not on absorption," *Optics Letters* **27**, pp. 731–733 (2002).

[25] Elaloufi, R. and Carminati, R. and Grefet, J.-J., "Definition of the diffusion coefficient in scattering and absorbing media," *J. Opt. Soc. Am. A* **20**, pp. 678–685 (2003).

[26] Ntziachristos, V. and Ripoll, J. and Weissleder, R., "Would near-infrared fluorescence signals propagate through large human organs for clinical studies?," *Optics Letters* **27**, pp. 333–335 (2002).

[27] Franceschini, M. A. and Moesta, K. T. and Fantini, S. and Gaida, G. and Gratton, E. and Jess, H. and Mantulin, W. W. and Seeber, M. and Schlag, P. M. and Kaschke, M., "Frequency-domain techniques enhance optical mammography: Initial clinical results," *Proc. Natl. Acad. Sci.* **94**, pp. 6468–6473 (1997).

[28] Grosenick, D. and Wabnitz, H. and Rinneberg, H. and Moesta, K. and Schlag, P., "Development of a time domain optical mammograph and first in vivo applications," *Appl. Opt.* **38**, pp. 2927–2943 (1999).

[29] Ntziachristos, V. and Tung, C. and Bremer, C. and Weissleder, R., "Fluorescence molecular tomography resolves protease activity in vivo," *Nature Med* **18**, pp. 757–760 (2002).

[30] Ntziachristos, V. and Weissleder, R., "CCD-based scanner for three-dimensional fluorescence-mediated diffuse optical tomography of small animals," *Medical Physics* **29**, pp. 803–809 (2002).

[31] Ntziachristos, V. and Bremer, C. and Graves, E. E. and Ripoll, J. and Weissleder, R., "In vivo tomographic imaging of near-infrared fluorescent probes," *Molecular Imaging* **1**, pp. 82–88 (2002).

[32] Graves, E. E. and Ripoll, J. and Weissleder, R. and Ntziachristos, V., "A submillimeter resolution fluorescence molecular imaging system for small animal imaging"," *Medical Physics* **30**, pp. 901–911 (2003).

[33] K. M. Case and P. F. Zweifel, *Linear Transport Theory*. MA: Addison-Wesley (1967).

[34] A. Ishimaru, "Difference between Ishimaru's and Furutsu's theories on pulse propagation in discrete random media," *J. Opt. Soc. Am. A* **1**, pp. 506–509 (1984).

[35] Durduran, T. and Boas, D. A. and Yodh, A. G. and Chance, B., "Does the diffusion coefficient depend on absorption?," *J. Opt. Soc. Am. A* **14**, pp. 3358–3365 (1997).

[36] D. J. Durian, "The diffusion coefficient depends on absorption," *Opt. Lett.* **23**, pp. 1502–1504 (1998).

[37] M. Bassani, F. Martelli, G. Zaccanti and D. Contini, "Independence of the diffusion coefficient from absorption: experimental and numerical evidence," *Opt. Lett.* **22**, pp. 853–855 (1997).

[38] K. Furutsu, "Diffusion equation derived from space-time transport equation," *J. Opt. Soc. Am. A* **70**, pp. 360–366 (1980).

[39] D. A. Boas, M. A. O'Leary, B. Chance, and A. G. Yodh, "Scattering and wavelength transduction of diffuse photon density waves," *Phys. Rev. E* **47**, pp. R2999–R3002 (1993).

[40] M. A. O'Leary, D. A. Boas, B. Chance, and A. G. Yodh, "Refraction of diffuse photon density waves," *Phys. Rev. Lett.* **69**, pp. 2658–2661 (1992).

[41] R. Aronson, "Boundary conditions for diffusion of light," *J. Opt. Soc. Am. A* **12**, pp. 2532–2539 (1995).

[42] R. C. Haskell and Svaasand, L. O. and Tromberg, B. J., "Boundary conditions for the diffusion equation in radiative transfer," *J. Opt. Soc. Am. A* **11**, pp. 2727–2741 (1994).

[43] S. Ito, "Comparison of diffusion theories for optical pulse waves propagated in discrete random media," *J. Opt. Soc. Am. A* **1**, pp. 502–505 (1984).

[44] I. Freund and Kaveh, M. and Rosenbluh, M., "Dynamic multiple scattering: ballistic photons and the breakdown of the photon-diffusion approximation," *Phys. Rev. Lett.* **60**, pp. 1130–1133 (1988).

[45] K. M. Yoo and Liu, F. and Alfano, R. R., "When does the diffusion approximation fail to describe photon transport in random media?," *Phys. Rev. Let.* **64**, pp. 2647–2650 (1990).

[46] Papazoglou, T. G. and Liu, W. Q. and Vasiliou, A. and Grassmel, R and Papagiannakis, R. and Fotakis, C, "Limitations of diffusion approximation in describing femtosecond laser transillumination of highly scattering media of biological significance," *Appl. Phys. Lett.* **67**, pp. 3712–3714 (1995).

[47] Hielscher, A. H. and Alcouffe, R. E. and Barbour, R. L., "Comparison of finite-difference transport and diffusion calculations for photon migration in homogeneous and heterogeneous tissues," *Phys. Med. Biol.* **43**, pp. 1285–1302 (1998).

[48] N. G. Chen and J. Bai, "Monte carlo approach to modeling of boundary conditions for the diffusion equation," *Phys. Rev. Lett.* **80**, pp. 5321–4324 (1998).

[49] A. D. Kim and Ishimaru, A., "Optical diffusion of continuous-wave, pulsed, and density waves in scattering media and comparisons with radiative transfer," *Appl. Opt.* **37**, pp. 5313–5319 (1998).

[50] Pham, T. H. and Spott, T. and Svaasand, L. O. and Tromberg, B. J., "Quantifying the properties of two-layer turbid media with frequency-domain diffuse reflectance," *Appl. Opt.* **39**, pp. 4733–4745 (2000).

[51] Fishkin, J. B. and Fantini, S. and van de Ven, M. J. and Gratton, E., "Gigahertz photon density waves in a turbid medium: Theory and experiments," *Phys. Rev. E* **53**, pp. 2307–2319 (1996).

[52] Markel, V. A. and O'Sullivan, J. A. and Schotland, J. C., "Inverse problem in optical diffusion tomography," *J. Opt. Soc. Am. A* **20**, pp. 903–912 (2003).

[53] A. Banos, *Dipole radiation in the presence of a conducting half space.* New York: Pergamon (1966).

[54] X. De Li, T. Durduran, A. G.Yodh, B. Chance, and D. N. Pattanayak, "Diffraction tomography for biochemical imaging with diffuse-photon density waves," *Opt. Lett.* **22**, pp. 573–575 (1997).

[55] Colak, S. B. and Papaioannou, D. G. and van Asten, N. A. A. J., "Tomographic image reconstruction from optical projections in light-diffusing media," *Appl. Opt.* **36**, pp. 181–213 (1997).

[56] T. Durduran, J. P. Culver, M. J. Holboke, X. D. Li, L. Zubkov, B. Chance, D. N. Pattanayak and A. G. Yodh, "Algorithms for 3d localization and imaging using near-field diffraction tomography with diffuse light," *Opt. Exp.* **4**, pp. 247–262 (1999).

[57] Ripoll, J. and Carminati, R. and Nieto-Vesperinas, M., "Spatial resolution of diffuse photon density waves," *J. Opt. Soc. Am. A* **16**, pp. 1466–1476 (1999).

[58] Ripoll, J. and Ntziachristos, V. and Culver, J. P. and Pattanayak, D. N. and Yodh, A. G. and Nieto-Vesperinas, M., "Recovery of opical parameters in multiple layered diffusive media: Theory and experiments," *J. Opt. Soc. Am. A* **18** (2001).

[59] J. Ripoll and M. Nieto-Vesperinas, "Reflection and transmission coefficients for diffuse photon density waves," *Opt. Lett.* **24**, pp. 796–798 (1999).

[60] van Staveren, H. J. and Moes, C. J. and van Marle, J. and Prahl, S. A. and van Gemer, M. J. C., "Light scattering in Intralipid-10% in the wavelength range of 400-1100 nm," *Applied Optics* **30**, pp. 4507–4514 (1991).

[61] Flock, S. T. and Jacques, S. L. and Wilson, B. C. and Star, W. M. and van Gemert, M. J. C., "Optical properties of Intralipid: A phantom medium for light propagation studies," *Lasers in Surgery and Medicine* **12**, pp. 510–519 (1992).

[62] Moes, C. J. and van Gemert, M. J. C. and Star, W. M. and Marijnissen, J. P. A. and Prahl, S. A., "Measurements and calculations of the energy fluence rate in a scattering and absorbing phantom at 633 nm," *Applied Optics* **28**, pp. 2292–2296 (1989).

[63] L. G. Henyey and J. L. Greenstein, "Diffuse radiation in the galaxy," *AstroPhys. J.* **93**, pp. 70–83 (1941).

[64] Cubeddu, R. and Pifferi, A. and Taroni, P. and Torricelli, A. and Valentini, G., "A solid tissue phantom for photon migration studies," *Phys. Med. Biol.* **42**, pp. 1971–1979 (1997).

[65] Torricelli, A. and Pifferi, A. and Taroni, P and Giambattistelli, E. and Cubbedu, R., "In vivo optical characteriation of human tissues from 610nm to 1010nm by time-resolved reflectance spectroscopy," *Phys. Med Biol.* **46**, pp. 2227–2237 (2002).

[66] Swartling, J. and Dam, J. S. and Andersson_Engels, S., "Comparison os spatially and temporally resolved diffuse-reflectance measurement systems for determination of biomedical optical properties," *Appl. Opt. in press* (2003).

[67] Kienle, A. and Patterson, M. S., "Improved solutions of the steady-state and the time-resolved diffusion equations for reflectance from a semi-infinite turbid medium," *J. Opt. Soc. Am. A* **14**, pp. 246–254 (1997).

[68] Suzuki, K. and Yamashita, Y. and Ohta, K. and Kaneko, M. and Yoshida, M. and Chance, B., "Quantitative measurement of optical parameters in normal breasts

using time-resolved spectroscopy: in vivo results of 30 Japanese women," *J. Biomed. Opt.* **1**, pp. 330–334 (1996).

[69] Kang, K. A. and Chance, B. and Zhao, S. and Srinivasan, S. and Patterson, E. and Trouping, R., in *Photon Migration and Imaging in Random Media and Tissues* ( ), vol. 1888, pp. 487–499, "Breast tumour characterization using near infra-red spectroscopy,", Bellingham, WA: SPIE (1993).

[70] Troy, T. L. and Page, D. L. and Sevick-Muraca, E., "Optical properties of normal and diseased breast tissue: prognosis for optical mammography," *J. Biomed. Opt.* **1**, pp. 342–355 (1996).

[71] Gayen, S. K. and Alfano, R. R., "Sensing lesions in tissues with light," *Opt. Exp.* **4**, pp. 475–480 (1999).

[72] Bevilacqua, F. and Marquet, P. and Coquoz, O. and Depeursinge, C., "Role of tissue structure in photon migration through breast tissues," *Appl. Opt.* **36**, pp. 44–48 (1997).

[73] Wheater, P. R. and Burkitt, H. G. and Stevens, A. and Lowe, J. S., *Basic Histopathology*, ch. 17, pp. 190–196. CHURCHILL LIVINGSTONE.

[74] Thomsen S. and Tatman D., "Physiological and pathological factors of human breast disease that can influence optical diagnosis," *Adv. Opt. Biop. Opt. Mammography, Ann N. Y. Acad. Sci.* **838**, pp. 171–193 (1998).

[75] Cubeddu, R. and D'Andrea, C. and Pifferi, A. and Taroni, P. and Torricelli, A. and Valentini, G., "Effects of the menstrual cycle on the red and near-infrared optical properties of the human breast," *Photochem. Phobiol.* **72-73**, pp. 383–391 (2000).

[76] Cerussi, A. E. and Berger, A. J. and Bevilacqua, F. and Shah, N. and Jakubowski, D. and Butler, J. and Hilcombre, R. F. and Tromberg, B. J., "Sources of absorption and scattering contrast for near-infrare optical mammography," *Acad. Radiology* **8**, pp. 211–218 (2001).

[77] Duck, F. A., *Physical Properties of Tissue*, pp. 319–328. London: Academic (1990).